Remote Sensing of Environment 263 (2021) 112541

Contents lists available at ScienceDirect

Remote Sensing of Environment

journal homepage: www.elsevier.com/locate/rse

Temporal evolution of aerosols and their extreme events in polluted Asian regions during Terra's 20-year observations

Zhiyuan Hu[a,b], Qinjian Jin[c,*], Yuanyuan Ma[d], Bing Pu[c], Zhenming Ji[a,e], Yonghong Wang[f], Wenjie Dong[a,b]

[a] *School of Atmospheric Sciences, Key Laboratory of Tropical Atmosphere-Ocean System, Ministry of Education, Sun Yat-sen University, Zhuhai 519082, China*
[b] *Southern Marine Science and Engineering Guangdong Laboratory, Zhuhai 519082, China*
[c] *Department of Geography and Atmospheric Science, University of Kansas, KS 66045, USA*
[d] *Key Laboratory of Land Surface Process and Climate Change in Cold and Arid Regions, Northwest Institute of Eco-Environment and Resources, Chinese Academy of Sciences, Lanzhou 730000, China*
[e] *Key Laboratory of Meteorological Disaster (KLME), Ministry of and Education and Collaborative Innovation Center on Forecast and Evaluation of Meteorological Disasters (CIC-FEMD), Nanjing University of Information Science and Technology, Nanjing, China*
[f] *Institute for Atmospheric and Earth System Research/Physics, Faculty of Science, P.O. Box 64, 00014 University of Helsinki, Helsinki, Finland*

ARTICLE INFO

Editor: Jing M. Chen

Keywords:
Trend
Aerosol
Extreme events
Radiation
Air pollution
Asia
Terra
MERRA-2

ABSTRACT

Aerosol pollution is an acute environmental issue in developing countries. Asia has been experiencing rapid changes in anthropogenic aerosols during the past two decades due to fast growth in population and economy. It is still an open question how aerosol loadings, represented by aerosol optical depth (AOD), have evolved in this century, particularly during the past decade when China and India implemented a clean air act aiming to improve air quality. Based on Terra aerosol retrievals and aerosol reanalysis, a change point of AOD trend is detected at 2010 in East China versus a persistent increasing AOD trend in the Indian subcontinent with no detectable change point from 2000 to 2019. In East China, positive AOD trend (+0.11 ± 0.022 decade^{-1}) is confirmed from 2000 to 2010 (hereinafter the former period) yet negative trend (−0.26 ± 0.027 decade^{-1}) is identified from 2011 to 2019 (hereinafter the later period). In the Indian subcontinent, persistent positive trend (+0.04 ± 0.001) is detected from 2000 to 2019 (hereinafter the whole period). All of these trends are attributed mainly to changes in sulfate aerosols. Further analysis of the aerosol pollution extreme events (APEE; defined as daily AOD over the long-term local 90th AOD percentile) manifest a positive trend (+0.16 ± 0.029 decade^{-1}) of the APEEs' magnitude in East China during the former period yet a negative trend (−0.11 ± 0.020 decade^{-1}) during the latter period; the Indian subcontinent demonstrates a positive trend (+0.02 ± 0.004 decade^{-1}) during the whole period due to increasing sulfate aerosols. The APEEs have become more frequent (+3.5 ± 0.53 day month^{-1} decade^{-1}) in East China during the former period yet less frequent (−3.6 ± 0.39 day month^{-1} decade^{-1}) during the latter period; in the Indian subcontinent, more frequent APEEs (+1.1 ± 0.25 day month^{-1} decade^{-1}) have been detected during the whole period. Consistent with the AOD trends, clear-sky radiation in East China shows a negative trend at the surface (−3.2 ± 0.67 W m^{-2} decade^{-1}), a positive trend in the atmosphere (+1.4 ± 0.68 decade^{-1}), and a negative trend at the top of the atmosphere (−1.8 ± 0.43 decade^{-1}) during the former period, respectively; opposite trends with much larger magnitude are seen during the latter period. In the Indian subcontinent, the clear-sky radiation trends during the whole period are −1.4 ± 0.38, +1.7 ± 0.31, and + 0.5 ± 0.16 W m^{-2} decade^{-1} at the surface, in the atmosphere, and at the top of the atmosphere, respectively. Comparison of radiation trends at clear-sky and all-sky conditions suggests that absorbing aerosols dominate the radiation budget in the atmosphere and the aerosol reanalysis of the Modern-Era Retrospective Analysis for Research ans Applications version 2 (MERRA-2) might overestimate the radiation response to clouds. This study provides an up-to-date analysis of the long-term trends in aerosols and their extreme events and radiation in two of the world's heavily polluted regions and the results have important implications for assessment of the environmental and climatic impacts of the ongoing clean air acts in Asia.

---

* Corresponding author.
E-mail address: jqj@ku.edu (Q. Jin).

https://doi.org/10.1016/j.rse.2021.112541
Received 7 July 2020; Received in revised form 15 May 2021; Accepted 28 May 2021

1. Introduction

Atmospheric aerosols are tiny liquid, solid, or mixed-phase particles suspended in air with diameters ranging from several nanometres to about hundred micrometres. High aerosol concentrations could cause severe environmental issues and disasters, which could further result in severe health problems, such as reproductive effects and respiratory problems (Burnett et al., 2018; Landrigan et al., 2018; Balakrishnan et al., 2019; Goldman and Dominici, 2019). Moreover, atmospheric aerosols can modulate Earth's climate system by 1) directly interacting with solar radiation and to a lesser extent with terrestrial radiation through absorption and scattering (Jin et al., 2016a; Satheesh and Krishnamoorthy, 2005; Yang et al., 2018a; Zhao et al., 2020), and 2) interacting with clouds by serving as cloud condensation nuclei and ice nuclei on which cloud droplets and ice crystals form (Fan et al., 2016; Qiu et al., 2017; Li et al., 2018; Zhao et al., 2018). They can be directly emitted from natural or anthropogenic sources (i.e., primary aerosols) or converted from gases (i.e., secondary aerosols). Due to natural variability of climate system and changing environmental policies across the globe, atmospheric aerosols demonstrate a large spatial heterogeneity and temporal variation (Che et al., 2019; Wei et al., 2019), particularly in Asia because of rapid development of industrialization and urbanization during the past several decades (e.g., An et al., 2019). Therefore, monitoring long-term changes of aerosol abundances has important implications for evaluating the effectiveness of environmental policies and their associated climatic impacts.

However, there are few long-term (e.g., decades) observations of aerosol properties at global scale. The AErosol RObotic NETwork (AERONET), which is a quasi-global (ground-based) network of sun photometers measuring atmospheric aerosol properties (Holben et al., 1998), has been providing long-term aerosol observations with high accuracy and thus been widely used as ground truth to evaluate uncertainties of other aerosol observations, such as satellite retrievals (Liu and Mishchenko, 2008; Mishchenko et al., 2009; Mishchenko et al., 2010; Yang et al., 2019; Yang et al., 2020). However, AERONET datasets lack observations over oceans and suffer great spatial heterogeneity over land. Most of AERONET sites locate in or near urban areas in developed countries (e.g., the United States and Europe) while very few sites are deployed in regions with frequent and intense natural aerosol pollution events (Martins et al., 2019; Pokharel et al., 2019), such as Africa, the Arabian Peninsula, Central Asia, West China, Russia, and Australia. More importantly, during the 27 years (1993–2019) of observation timespan, there are fewer than 50 AERONET sites that have a data coverage longer than 15 years (Ningombam et al., 2019). Therefore, although AERONET have been providing valuable and unique observations of aerosol properties during the past three decades or so, it is not suitable for study of long-term changes of aerosol pollutants at global scale.

Satellite remote sensing is the only available method to retrieve long-term aerosol properties over the globe except high latitude (i.e., $> \sim 80^\circ$) regions due to high reflectance of snow/ice surface and large solar zenith angle (Kokhanovsky and Leeuw, 2009). Satellite remote sensing of atmospheric aerosols can go back to 1970s, since when a number of satellite platforms and sensors have been developed and their products have been widely used in atmospheric and environmental communities (Hsu et al., 1999; Sayer et al., 2012; Hsu et al., 2017; Wang et al., 2018; Peng et al., 2020). Among the numerous satellites, Terra is the one that has been in orbit for more than 20 years and thus is selected to study the decadal trends of atmospheric aerosols. Launched in December 1999, the National Aeronautics and Space Administration (NASA) Terra satellite carries two sensors that have provided global and daily measurements of aerosols for long-term monitoring of environmental and climate changes. Owning to unique design, such as multiangle or multispectral, the Moderate Resolution Imaging Spectroradiometer (MODIS) and the Multiangle Imaging Spectroradiometer (MISR) have been providing high-quality AOD data starting from February 24, 2000 to present (Sayer et al., 2019; Garay et al., 2020). A number of important findings in environmental and climate sciences could not be achieved without long-term Terra-MODIS and MISR AOD (jointly referred to Terra AOD hereafter). Terra AOD have been widely used to estimate the particulate matter with a mass median aerodynamic dimeter of <2.5 μm ($PM_{2.5}$) on global scale (van Donkelaar et al., 2006; van Donkelaar et al., 2010), which have significantly advanced the studies of relationship between long-term exposure to air pollution and mortality (Di et al., 2016; van Donkelaar et al., 2016; Di et al., 2017). Moreover, using Terra AOD, interactions among environmental policies, aerosol abundances, and climate systems have been intensely studied. Statistically significant positive correlations, for instance, were found between Terra AOD over the Middle East and the Indian summer monsoon precipitation during the past two decades or so (Jin et al., 2014; Vinoj et al., 2014), which have stimulated a large number of studies aiming to reveal the physical mechanisms behind the observed correlations (Jin et al., 2015; Solmon et al., 2015; Jin et al., 2016b; Jin et al., 2021; Sharma and Miller, 2017; Kumar and Arora, 2018). Another important application of Terra AOD is detection and attribution of long-term trends of AOD in regions across the globe, such as at global scale (de Meij et al., 2012; Hsu et al., 2012; Mehta et al., 2016; Che et al., 2019; Wei et al., 2019; Yu et al., 2020), global oceanic regions (Zhang and Reid, 2010), the Middle East (Klingmüller et al., 2016; Pu and Ginoux, 2016; Jin et al., 2018), India (Kaskaoutis et al., 2011; Ramachandran et al., 2012; Jethva et al., 2018; Jin and Wang, 2018; Prijith et al., 2018), United States (Yang et al., 2018b; Jin et al., 2020; Jin and Pryor, 2020), and global megacities (Alpert, 2012; Shen and Zhao, 2020). Overall, aerosol data from Terra mission have made tremendous contribution to scientific communities of environment and climate during the past two decades.

However, because Terra AOD are not retrieved over cloudy or ice/snow or sun glint regions (Hsu et al., 2013; Garay et al., 2020), most of the abovementioned studies used monthly AOD data to get a larger spatial coverage than using daily data. Such drawback of Terra AOD introduces time representation errors (Wang and Zhao, 2017) and also preclude studies of aerosol pollution extreme event (APEE; defined as daily AOD above the local 90th percentile), which usually have a lifetime ranging from hours to days and thus requires AOD data of high temporal frequency (e.g., daily). The APEEs have great adverse health effects and are difficult to predict due to their sudden burst and thus could cause staggering economic loss (Jaramillo and Muller, 2016) and millions of premature mortalities (Lelieveld et al., 2015; Burnett et al., 2018; Lelieveld et al., 2019; Liu et al., 2019), but they are under-examined in terms of spatial patterns and long-term trends because of a lack of aerosol observations with high temporal frequency.

Data assimilation is a powerful and objective technique which combines observational data (e.g., satellite) and the underlying dynamical principles governing the climate system (i.e., model output) to determine an optimal possible state of the climate system (e.g., Lahoz and Schneider, 2014). One of the advantages of this methodology is filling in the spatiotemporal gaps in observations. Therefore, it is widely applied in the investigations of the climate system, including aerosols (e.g., Tang et al., 2017; Pathak et al., 2019). Modern-Era Retrospective Analysis for Research and Applications version 2 (MERRA-2) is a reanalysis produced by the Goddard Earth Observation System (GEOS-5.12.4) atmospheric model and the Gridpoint Statistical Interpolation analysis for data assimilation (Rienecker et al., 2011; Gelaro et al., 2017). It is the first long-term (1980–present) global reanalysis which assimilates multiple satellite observations of aerosols, including MISR, MODIS aboard both Terra and Aqua, the Advance Very High Resolution Radiometer (AVHRR) as well as AERONET station observations (Randles et al., 2016; Randles et al., 2017). The hourly output of aerosol properties from MERRA-2 overcomes one of the drawbacks of satellite data (i.e., missing values) and thus provides the first opportunity to study the long-term trends of APEEs at global scale.

East China and the Indian subcontinent have been suffering the acutest air pollution problem during the past two decades. Together accounting for about 40% of the global population and having the rapid economic growth (Fig. 1), those two regions emit millions of tons of air pollutants every year, which makes them two of the world's most polluted places (Lelieveld et al., 2015; Burnett et al., 2018; Weagle et al., 2018). To reduce the health impact of air pollutants, both countries have introduced measures to limit air pollution emissions from automotive emissions, coal heating, polluting industries, and construction sector during the past decade (Sundaray and Bhardwaj, 2019; Zhang et al., 2019b). These measurements have been shown to make a great effect in mitigating the air pollution in China (Li et al., 2019; Zhai et al., 2019; Zhang et al., 2019b; Fan et al., 2020), but it is still an open question how the air pollution in India has been evolved during the past two decades (Pant et al., 2018; Samset et al., 2019). More importantly, previous studies have focused on the temporal changes of the mean status of the air pollution, but few studies, to our knowledge, have addressed the long-term changes of the air pollution peaks, or the APEEs, which have great adverse impact on human health and traffic safety.

In this study, using Terra MISR and MODIS aerosol retrievals and the MERRA-2 reanalysis, we first detected a change point of AOD trends at the year of 2010 in East China but no change point in the Indian subcontinent. Then we estimated and compared the long-term trends in AOD in East China during two periods: March 2000–February 2011 (2000−2010) and March 2011–February 2020 (2011–2019) (hereafter, the former and later periods) and in the Indian subcontinent during the period of March 2000–February 2020 (2000–2019) (hereafter, the whole period). Such comparisons can help us better understand 1) how much the air quality has been improved since China released its Air Pollution Action Plan in 2013 and the Three-year Action Plan for Winning the Blue Sky War in 2018; and 2) what experience countries in the Indian subcontinent can learn from China to significantly improve their air quality. Second, we for the first time defined the APEE using daily MERRA-2 data and quantified the trends in the terms of magnitude and frequency of APEEs in these two regions. Last, employing the Clouds and the Earth's Radiant Energy System (CERES) data, we addressed the response of the shortwave radiation to the AOD trends at the top of the atmosphere, in the atmosphere, and at the surface in these two regions.

2. Datasets

2.1. Terra mission

NASA's Earth Science Division, supported by Congress, is a Presidential Initiative with dedication to a better understanding of the integrated Earth system and natural and human-induced long-term changes on the global environment. As the centrepiece of the Earth Science Division, the Earth Observation System (EOS) is a series of polar-orbiting satellites for global observations of land surface, atmosphere, oceans, biosphere, and cryosphere. Terra is the “flagship” satellite of the Earth Observing System. It was launched on December 18, 1999 and started collecting data on February 24, 2000. It is operating in a polar sun-synchronous orbit at 705 km above the Earth's surface and circle the Earth by 16 times every day, so at any given latitude it flies directly overhead at the same time each day. It crosses the equator on descending passes (i.e., north to south) at 10:30 a.m. local time when the global land is generally covered by less clouds than in the afternoon hours during a day (Gristey et al., 2018). There are five instruments aboard Terra, three of which are used in this study—MODIS, MISR, and CERES (Table 1).

2.1.1. Terra-MODIS

The MODIS instrument onboard the Terra satellite observes the Earth system in 36 spectral bands and provides a nearly global coverage within 1–2 days owing to its wide swath of 2330 km (King et al., 1999). The aerosol properties, such as AOD, are retrieved from three algorithms: dark target (DT) over vegetated lands (NDVI $\geq$0.1), DT over waters, and deep-blue (DB) over bright lands (e.g., desert) (Kaufman et al., 1997; Hsu et al., 2004; Remer et al., 2005; Hsu et al., 2006; Levy et al., 2007). The above algorithms have been continuously improved to retrieve higher quality aerosol products. In MODIS collection 6.1, the DT land algorithm is updated to reduce the biases in urban areas based on a surface reflectance model (Gupta et al., 2016), and the DB land algorithm is updated to produce a dynamic surface reflectance dataset depending on the normalized difference vegetation index (NDVI) and a pre-calculated surface reflectance database. More importantly, the DB retrievals expand its spatial coverage from arid and semi-arid regions to the entire land areas (Hsu et al., 2013). To increase the data spatial coverage, a “merged” monthly dataset of AOD at 550 nm of collection 6.1 combined DT and DB retrievals is employed herein (Levy et al., 2013; Sayer et al., 2014). Over land, where NDVI $\leq$0.2 in a given month,

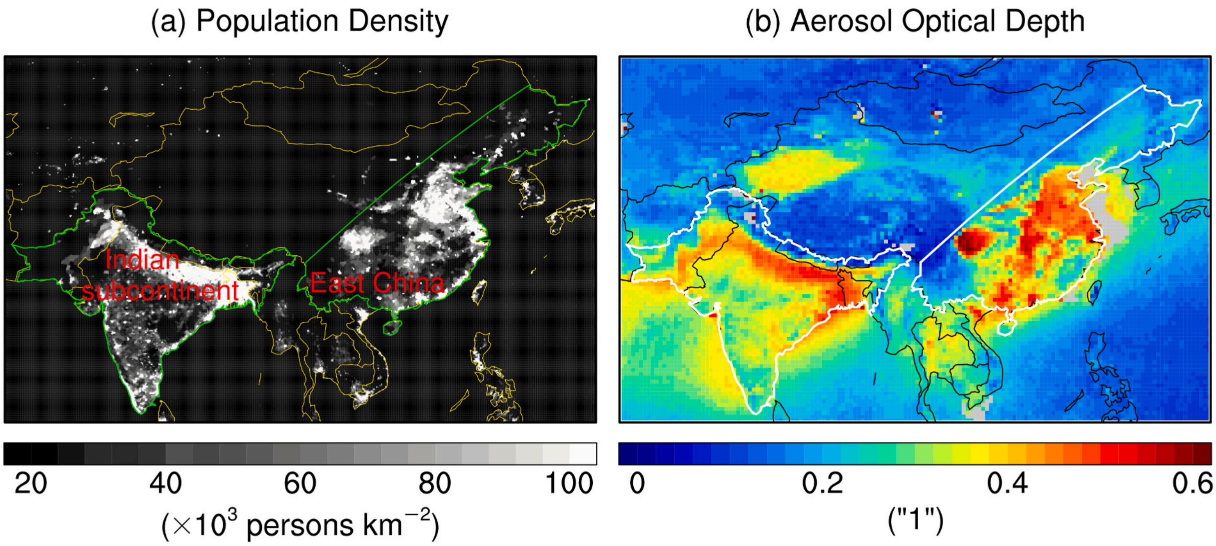

Fig. 1. The spatial patterns of (a) population density ($\times10^3$ persons km^{-2}) and (b) aerosol optical depth. The population data are for the year of 2000 and the aerosol data are from MISR level 3 dataset from 2000 to 2019. East China and the Indian subcontinent are outlined for further analyses. Grey colors in panel (b) represent missing values.

Table 1
Summary of datasets analyzed in this study. AOD is retrieved at 550 nm in all datasets in this study.

Dataset	Version	Variable	Period	Resolution		Download Link
				Temporal	Spatial (lon. × lat.)	
MISR	V32	AOD	2000.03–2020.02	Monthly	1/2° × 1/2°	https://l0dup05.larc.nasa.gov/opendap/misrl2l3/MISR/MIL3MAEN.004/
MODIS (MOD08_M3)	V61	AOD	2000.03–2020.02	Monthly	1° × 1°	https://ladsweb.modaps.eosdis.nasa.gov/archive/allData/61/MOD08_M3
MERRA-2	V2	AOD	2000.03–2020.02	Monthly and daily	5/8° × 1/2°	https://goldsmr5.gesdisc.eosdis.nasa.gov/opendap/MERRA-2
CERES (EBAF)	Ed4.1	Radiation	2000.03–2020.02	Monthly	1° × 1°	https://ceres.larc.nasa.gov/order_data.php
SEDAC	v1.01	Population	2000	Annual	1/8° × 1/8°	https://sedac.ciesin.columbia.edu/data/set/popdynamics-1-8th-pop-base-year-projection-ssp-2000-2100-rev01/data-download

the DB AOD is aggregated to get the "merged" AOD, and where NDVI ≥0.3, the DT AOD is used. For intermediate NDVI, the AOD with higher quality flag is used; in the case of the same quality flag, the mean is used. The monthly data in collection 6.1 have a spatial resolution of 1° × 1° and cover a period from March 2000 to February 2020 for MODIS-Terra.

2.1.2. Terra-MISR

The MISR instrument onboard the Terra satellite observes the Earth with nine cameras oriented along the satellite track with five view angles relative to the Earth's (Diner et al., 1998). The nine cameras observe the Earth at 4 spectral bands. Using the multi-angle and multi-spectrum in the MISR instrument, various aerosol properties can be retrieved in high accuracy. Over land, a dense dark vegetation (DDV) algorithm and the spatial contrasts are used to retrieve the aerosol properties (Martonchik et al., 2009). The DDV algorithm assumes the surface reflectance at each wavelength for those vegetation areas identified by large NDVI values (King et al., 1992) and empirical orthogonal functions constructed from the radiances at the individual pixels in a satellite image are used to describe surface constrast of the observed radiance (Martonchik, 1997). Over dark water, a forward radiative transfer model is used to retrieve aerosol properties with an assumption of water bodies to be a blackbody at the red and near-infrared wavelengths (Kalashnikova et al., 2013; Wei et al., 2019). Because of the narrower swath of 380 km than MODIS (i.e., 2330 km), the MISR covers the global in a longer period of ~9 days than MODIS (i.e., 1–2 days). Therefore, MISR level 3 monthly aerosol products are usually used to study the long-term variations in AOD because the daily aerosol products have missing values over about 90% of global areas (e.g., Jin et al., 2018). In this study, the newly released MISR monthly AOD with retrieval algorithm version 23 and data format version 15 (F15_0032) are used. A number of updates have been implemented in the new dataset, such as mitigating the existence of a gap in AOD between 0.0 and 0.02 and reducing the stray light effects induced by internal reflections among MISR cameras. The monthly data have a spatial resolution of 0.5° × 0.5° and cover a period from March 2000 to February 2020. Note that the previous version (F08_0031) of MISR retrievals reports AOD at 555 nm, while the new version (F15_0032) reports AOD at 550 nm, which facilitates direct comparison of MISR AOD with other AOD data, such as MODIS and MERRA-2. A detailed introduction to the latest MISR dataset can be found in Garay et al. (2020).

The foregoing factors that contribute to the differences between Terra-MODIS and Terra-MISR AOD products are summarized as follows: sampling differences that are determined by orbital coverage (i.e., sensor swath width), retrieval algorithm differences, different strategies for spatial aggregation and temporal averaging from swath products (e.g., daily level 2) to gridded global products (e.g., monthly level 3) (Levy et al., 2015). All these factors could cause differences in the AOD trends estimated using the two AOD datasets. Note that the orbital drift in the first two years of Terra mission should not affect our trend estimation because no drift was detected in Terra MODIS and MISR AOD in the first two years (Zhang and Reid, 2010; Sayer et al., 2019; Garay et al., 2020).

2.1.3. Terra-CERES

The CERES instruments aboard Terra are used to measure the Earth's radiation energy budget and cloud properties in 12 longwave and 15 shortwave spectral bands. The radiation fluxes at the Earth's surface and at the top of atmosphere (TOA) are assessed using delta-two stream radiation transfer model (Fu and Liou, 1993) under cloudy-sky (with clouds and aerosols) and clear-sky (without clouds and aerosol). The CERES could provide 3-h synoptic, daily, monthly, and yearly products with horizontal resolution of 140 km × 140 km (Wielicki et al., 1996). The TOA radiation fluxes are retrieved through combined with the production from the Tropical Rainfall Measuring Mission (TRMM; November 1997 onwards), Terra (March 2000 onwards), Aqua (July 2002 onwards), Suomi National Polar-orbiting Partnership (S-NPP; January 2012 onwards), and Joint Polar Satellite System (JPSS). The AOD products from MODIS on Terra and Aqua, and the cloud properties from MODIS on Terra and Aqua and the Visible Infrared Imaging Radiometer Suite (VIIRS) on S-NPP are used (Hsu et al., 2004, 2006; Minnis et al., 2008; Remer et al., 2008; Levy et al., 2013). Moreover, the atmosphere constituents and aerosol properties are from the Model for Atmospheric Transport and Chemistry (MATCH). The meteorological data, including precipitable water, skin temperature, and surface wind speed are from the GEOS-5.4.1 data assimilation system product (Remer et al., 2008). In this study, the monthly radiation fluxes productions during March 2000 to February 2020 are used, which are derived from Level 4 EBAF Ed2.6r products (https://ceres.larc.nasa.gov/order_data.php) with a spatial resolution of 1° × 1° (Loeb et al., 2018). Here, we have considered radiation fluxes at the surface, in the atmosphere (computed as a residual term), and at the TOA.

2.2. MERRA-2

MERRA-2 is the NASA's latest atmospheric reanalysis (Gelaro et al., 2017). It is produced by the Goddard Earth Observing System (GEOS-5.12.4) atmospheric data assimilation system. The system is composed of the GEOS atmospheric model (Molod et al., 2015) and the Gridpoint Statistical Interpolation (GSI) analysis scheme (Kleist et al., 2009). The GEOS-5 model simulates the atmospheric forecast with an approximate horizontal resolution of 0.5° latitude × 0.625° longitude using a cubed-sphere horizontal discretization. Following the success of the earlier MERRA analysis, the MERRA-2 analysis incorporates more new observation sources in the system and reduces spurious jumps and trends due to the changes in the meteorological observing system (McCarty et al., 2016; Gelaro et al., 2017). One of the most important updates in MERRA-2 is the assimilation of long-term aerosol observations from multiple satellite remote sensors (Randles et al., 2017). The assimilated aerosol observations include

- The neural net retrieval (NNR) AOD from AVHRR (1979–2002, ocean-only) retrieved from the recalibrated AVHRR pathfinder atmosphere-extended radiances against MODIS (Heidinger et al., 2002; Heidinger et al., 2014);
- The NNR AOD from MODIS aboard Terra (2000–present) and Aqua (2002–present) derived from collection 5 MODIS radiances (Remer et al., 2005; Levy et al., 2007);
- MISR official AOD of version 22 (2000–2014) only over bright surfaces (albedo >0.15) (Kahn et al., 2005), which stops on June 30, 2014.
- The cloud-screened level 2.0 AERONET AOD, which stops on October 29, 2014 (Holben et al., 1998; Smirnov et al., 2000).

The use of NNR AOD from AVHRR and MODIS instead of their official AOD data in the assimilation system is to correct the biases in AOD data (Randles et al., 2016; Randles et al., 2017). To the best of our knowledge, MERRA-2 is the first multidecadal reanalysis, in which both aerosol and meteorological observation were assimilated, and aerosol-radiation interaction is represented by the Goddard Chemistry, Aerosol, Radiation, and Transport model (GOCART) (Gelaro et al., 2017). GOCART model simulates five aerosol species, including mineral dust, sulfate, black carbon (BC), organic carbon (OC), and sea-salt. Both sulfate and carbonaceous aerosol emissions is primary from biomass burning, fossil fuel combustion, and biofuel consumption (Randles et al., 2016). The dust and sea-salt emissions are driven based on wind speed following Marticorena and Bergametti (1995) and Gong (2003), respectively. Moreover, the secondary chemical oxidation of sulfur dioxide (SO_2) and volcanic SO_2 emissions are also included (Randles et al., 2017). Comparison of MERRA-2 AOD with AERONET observations during 1993–2016 demonstrated a good spatial agreement across the globe with a spatial correlation of 0.85 and root-mean-square error of 0.12 (Che et al., 2019). It is pertinent to note that only total AOD in MERRA-2 is constrained by assimilating satellite retrievals and the AODs of various aerosol species are determined by the model emission inventories and meteorology.

Here, we use both daily (averaged for 24 h a day) and monthly AOD at 550 nm in MERRA-2 for total aerosols and aerosol species to analyse the long-term trends for both climatological and APEE AOD. In order to match the satellite observation, the study period is March 2000 to February 2020.

2.3. *Population density*

The Global One-Eighth Degree Population Base Year and Projection Grids Based on the Shared Socioeconomic Pathways, Revision 01, dataset is used to demonstrate the spatial patterns of population density in East China and the Indian subcontinent (Jones and O'Neill, 2016). The data for the base year 2000 are used here to demonstrate the spatially close association between population and AOD in these two regions.

3. Methodology

3.1. *Definition of APEE*

The extreme event in climate science is usually defined as a time period (e.g., hours to years) when a meteorological condition is over or below some threshold values. Two widely used definitions can be distinguished based on whether the threshold is defined as a fixed value across the entire domain of interest (e.g., Roxy et al., 2017) or it is defined for each grid cell and thus varies across the domain (e.g., Jin and Pryor, 2020). The thresholds in both definitions are determined as a specific percentile of the meteorological variable along the time dimension during a climatological period, such as 30 years. The first definition is usually employed for simplicity when the meteorological condition in question shows a relatively uniform spatial pattern, while otherwise the second definition is used. In this study, given the large spatial variation of AOD in the study domain (Fig. 1), the second definition is employed. An APEE is defined as a day when the daily AOD is above the 90th percentile AOD for a grid cell and month, i.e., AOD $\geq P_{90,\ AOD}(m,i,j)$, where $P_{90,\ AOD}(m,i,j)$ is the 90th percentile of AOD at grid cell (i,j) in a specific month (m). In other words, $P_{90,\ AOD}(m,i,j)$ is calculated using daily AOD only in that month from March 2000 to February 2020, so there are 12 AOD thresholds for each grid cell, corresponding to 12 months. The purpose of defining $P_{90,\ AOD}$ for each month is to avoid misclassification of days in months of peak AOD as APEEs due to strong seasonal variations of AOD in the study domain (Fig. 1). Here, MERRA-2 daily AOD is used to select APEEs and then the monthly APEE AOD is calculated as the mean AOD from those days when AOD meets the APEE criteria (i.e., above the 90th percentile AOD) for each grid cell and month (Fig. S1). The monthly AOD that is averaged over all days versus APEEs alone in a month are marked as monthly all-day vs. monthly APEE AOD, respectively. The monthly APEE AOD shows large seasonal and temporal variations: relatively large values (~1) are found from January to April in East China, during summer monsoon season in the western Indian subcontinent due to strong dust emissions and during post-monsoon season in the northern Indian subcontinent due to anthropogenic emissions.

3.2. *Trend estimation and statistical testing*

The temporal trend is estimated using the linear least-squares regression method (Zwiers and Von Storch, 1995), which is a traditional method and has been widely used to estimate linear trends. The *p* values of the least-squares regression coefficients are evaluated using the two-tailed Student's *t*-test. Trends are computed at the annual timescales where the mean of monthly mean values are used. Therefore, the sample size is the number of years used in a trend estimation. Our analysis shows that the annual time serieses of AOD are not significantly autocorrelated at the 90% dofidence level. Therefore, the impact of autocorrelation on the trend estimation is neglected. Moreover, using the Kolmogorov–Smirnov test, we show that the residual errors of annual AOD from the fitted regression lines at all grid points in East China and Indian subcontinent are normally distributed during the two periods (i.e., 2000–2010 and 2011–2019), irrespective of AOD datasets (Fig. S1). Based on the above analyses, the assumptions about the linear least-squares regression method are reliable and thus can be safely applied in trend estimation.

To avoid overstatement and overintepretation of multiple simultaneous hypothesis testing results (e.g., statistical testing of trends in a number of geographical grid points) (Livezey and Chen, 1983), a method to control the fasle discovery rate (FDR) is applied to *p* values (Wilks, 2016). The method operates on the sorted *p* values in an increasing order, $p_{(1)} \leq p_{(1)} \leq \ldots \leq p_{(N)}$, from *N* local hypothesis tests and finds a threshold for the *p* values. The local null hypothesis that the local trends are zero are rejected if their *p* values are smaller than or eaqual to the threshold level p_{FDR}*, which is calculated using Eq. (1):

$$p_{FDR}^{*} = \max_{i=1,\ldots,N}\left[p_{(i)} : p_{(i)} \leq \left(\frac{i}{N}\right)\alpha_{FDR}\right] \tag{1}$$

where α_{FDR} is the chosen control level for the FDR and *i* is the rank. Note that there are various methods that can be used to determine p_{FDR}* (Simes, 1986; Benjamini and Hochberg, 1995; Wilks, 2006); the selection of Eq. (1) is to achieve a reasonable sensitivity of the procedure for detecting false null hypotheses. For instance, a too strict p_{FDR}* would result in missed rejections of false null hypotheses while a too loose p_{FDR}* would result in false rejections of true null hypotheses. Based on the conclusion that "*for grid points exhibiting moderate to strong spatial correlation, approximately correct global test levels can be produced using the FDR procedure by chossing* $\alpha_{FDR} = 2\alpha_{global}$" (Wilks, 2016), here α_{FDR} is set to 0.1 (i.e., $\alpha_{global} = 0.05$) so that the statistical significance of the global hypothesis tests is at 95% confidence level.

Since the least-squares regression method is sensitive to data outliers, two additional methods—the Theil-Sen trend estimation with the Mann-Kendall test and bootstrapping—are also employed to evaluate the robustness of the regression method. The Theil–Sen estimator reports the median of the slopes of all lines, each of which connects two points (Fernandes and Leblanc, 2005). The Theil–Sen trend significance is tested using the Mann-Kendall test, which is non-parametric or distribution free test (Mann, 1945; Kendall, 1955). The Mann-Kendall trend test can be used for as few as four samples. However, the probability of missing a true trend increases as the number of samples decreases; the recommended minimum number of samples is at least 8 to 10. Because the software we used (i.e., NCL—NCAR Command Language) to perform the Mann-Kendall test requires at least 10 values, the Mann-Kendall test is not applied to the latter period (2011–2019). Bootstrapping resamples the data with replacement to estimate the probability distribution function of trends and then calculate the *p* value as a two-tailed probability of finding a trend equal to zero. Here, datasets are resampled by 10,000 times for area-averaged time series and 1000 times for time series at each grid cell to reduce computing time. Our results show that the trends and the associated statisical significance estimated by FDR using *p* values calculated by the three methods are generally consistent in terms of both spatial patterns and magnitudes (shown in Section 4.2). Therefore, only trends estimated by the linear least-squares regresion method are shown in this paper.

3.3. Piecewise trend detection

A piecewise regression method is used to determine if there is a change of trend in a time series. First, a differential evolution method is used to search for a piecewise linear regression model in the global domain (e.g., through the entire time series) that minimize the sum of residual errors from the fitted piecewise regression model (Storn and Price, 1997). Here, a piecewise regression model with two segments is proposed, corresponding to AOD time series before and after the control measurements of air quality. Second, determine if each segment of the piecewise regression model has statistically different trends. If so, we conclude that a change of trend is detected and the point that links the two segments is the breakpoint.

4. Results

4.1. Spatial and seasonal characteristics of AOD

East China and the Indian subcontinent are characterized by high AOD with strong seasonality. Fig. 2 illustrates the spatial distribution of climatology AOD in four seasons from the retrievals of MISR and MODIS onboard Terra and the MERRA-2 reanalysis for the period of 2000 to 2019. All of the three datasets show consistent spatial patterns of AOD in East Asia and the Indian subcontinent. However, MODIS shows higher (+29%) climatological AOD values at annual timescale than MERRA-2 yet MISR demonstrates lower AOD values (−36%) than MERRA-2 over East China and Indian subcontinent with the largest AOD differences in

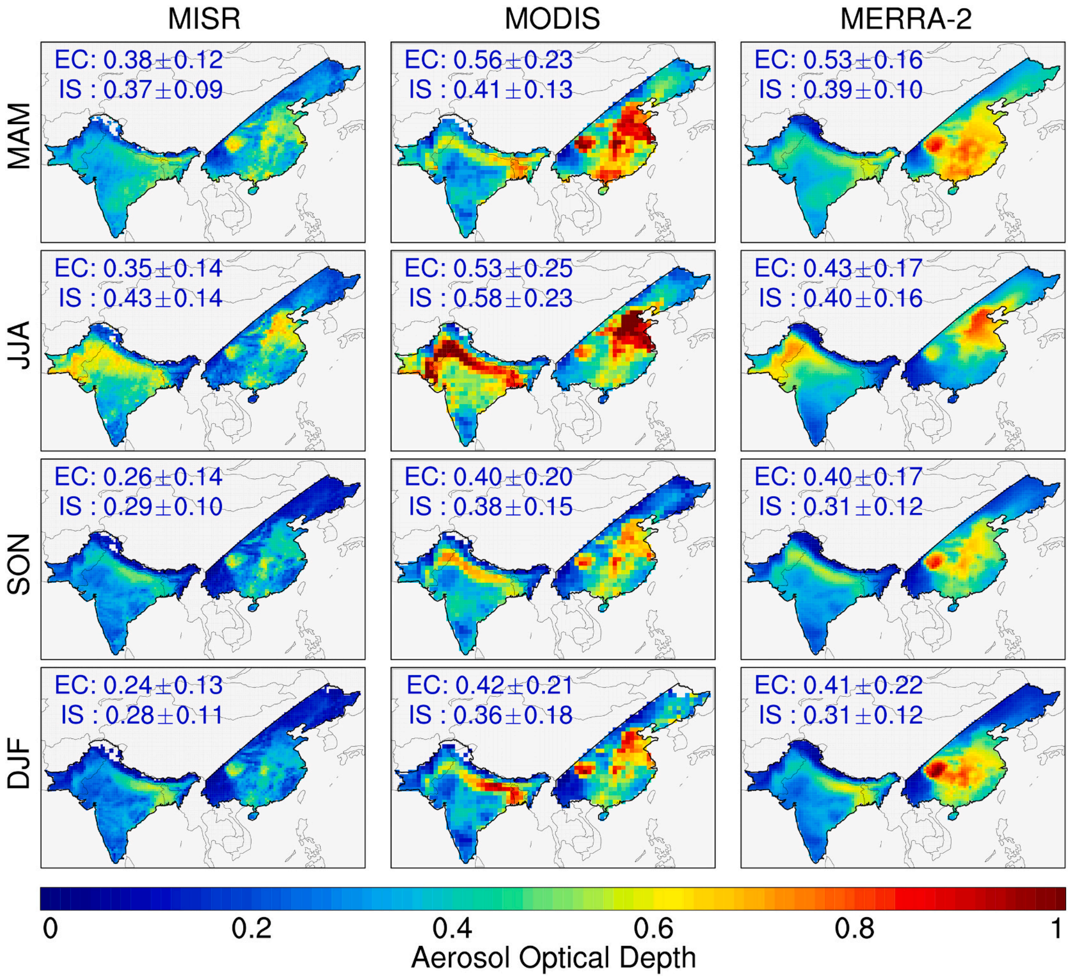

Fig. 2. Climatology (2000–2019) of seasonal aerosol optical depth in East China (EC) and the Indian subcontinent (IS). Data are from MISR and MODIS onboard Terra satellite and the MERRA2 reanalysis. The numbers in each panel represent the area-averaged aerosol optical depth and its spatial standard deviation.

the major anthropogenic polluted regions (i.e., Northern India and Eastern China). Overall, MODIS AOD is closer to MERRA-2 than MISR, particularly in regions of high AOD values, which could be partially attributed to much larger (~5 times) spatial coverage of MODIS AOD than MISR AOD (i.e., a swath width of 2330 km versus 380 km), meaning that MERRA-2 assimilates much more AOD data from MODIS than from MISR. Note that in the light of a fairly small absolute amount of assimilated AOD data due to the single overpass per sensor per day for locations in low and mid latitudes, it is also possible that the underlying GEOS model fields are more similar to MODIS in some areas. In general, the seasonal variabilities of AOD from the three datasets are similar in both regions with a peak value in summer (JJA, defined as June–July-August), followed by spring (MAM, defined as March–April-May). In JJA, the largest AOD occurs over the North China Plain and Sichuan Basin that is attributed to the anthropogenic pollutants emissions from local sources (Guo et al., 2011; Pozzer et al., 2015; Wei et al., 2019; Zhang et al., 2019a; Zhao et al., 2019) as well as in the Indo-Gangetic Plain that are attributed to both local anthropogenic emissions and remote natural dust aerosol emissions from the Thar Desert in Northwest India (Jin et al., 2014; Jin et al., 2015). The spatial averaged summertime AOD from MODIS is about 0.53 (0.35 from MISR; 0.43 from MERRA-2) in East Asia and 0.58 (0.43 from MISR; 0.40 from MERRA-2) in the Indian subcontinent. In MAM, the regions with larger AOD in East Asia extend to Southeast China with a spatial average of 0.56 from MODIS (0.38 from MISR; 0.53 from MERRA-2), and larger AOD occurs over the Indian subcontinent due to the anthropogenic pollutions with the spatial average of 0.41 from MODIS (0.37 from MISR; 0.39 from MERRA-2). In autumn (SON, defined as September–October-November) and winter (DJF, defined as December–January-February), the values of AOD are similar over the research domain with the spatial average of 0.36–0.42 from MODIS (0.24–0.29 from MISR; 0.31–0.41 from MERRA-2). Overall, the three datasets provide consistent AOD climatology in terms of both spatial distributions and seasonal variabilities.

The MERRA-2 data further provide aerosol species AOD for sulfate, OC, BC, dust, and sea-salt, which can help understand the relative contributions of each aerosol species to total AOD. Fig. 3a–f shows the spatial distributions of annual climatological AOD from individual aerosol species. Apparently, sulfate aerosols dominate the total AOD over East China and North and East India with a spatial averaged value of 0.29 and 0.13, respectively. The high dust AOD (about 0.12) mainly occurred over the Thar desert in the northwest the Indian subcontinent. Contributions from other aerosol species are very small. Overall, there are significant aerosol pollution in East Asia and the Indian subcontinent with the spatial averaged values of 0.44 and 0.35, respectively. In order to better understand the contribution of aerosol species to total AOD, the annual and seasonal AOD fractions of each aerosol species are shown in Fig. 3g–h. In East China, sulfate contributes about 65% to annual total AOD, followed by OC (15%) and dust (11%). In the Indian subcontinent, sulfate contributes about 38% to the annual total AOD, followed by dust (34%) due to the stronger dust emission over the Thar desert and organic carbon. Sea-salt accounts for a larger fraction (~13%) than black and organic carbons in summer in the Indian subcontinent, which is due to the strong southwest summer monsoon circulation that can generate high emissions of sea-salt aerosols and further transport them from the Arabian Sea northeastward to the Indian subcontinent (Jin et al., 2014). In East China, the largest contribution of aerosol specie is sulfate with a peak value of 72% in JJA and SON, and the second is OC with a peak of 21% in MAM. Differently, in the Indian subcontinent, dust has the

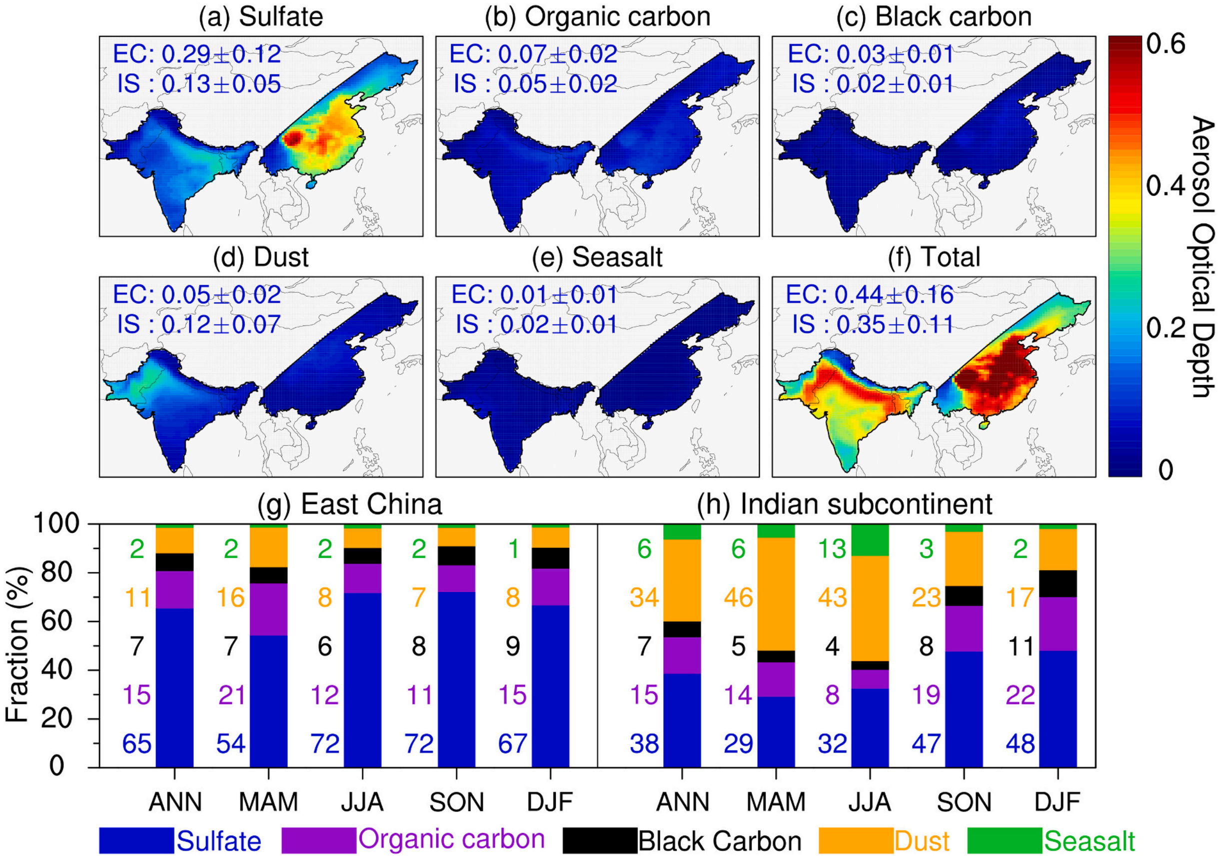

Fig. 3. Climatology (2000–2019) of aerosol optical depth (AOD) for each aerosol species. (a)–(f): Spatial patterns of AOD for five aerosol species and total aerosols at annual timescale. (g)–(h): Area-averaged fractions of five aerosol species in East China (EC) and the Indian subcontinent (IS) at annual and seasonal timescales. Data are from the MERRA2 reanalysis. The numbers in panels (a)–(f) represent the area-averaged AOD and its spatial standard deviation and the numbers in panels (g)–(h) are fractions of AOD for each aerosol species.

largest contribution in MAM (46%) and JJA (43%), while sulfate has the largest contribution in SON (47%) and DJF (48%). It is worth noting that the seasonal variabilities in aerosol species AOD are larger in the Indian subcontinent than in East China, due to strong dust emissions caused by the Indian summer monsoon.

4.2. AOD trend

Significant trends in AOD are detected in East China and the Indian subcontinent during the past two decades (2000–2019, as shown in Fig. 4). MISR and MODIS exhibit consistent negative-positive northeast-southwest differences in AOD trends in the study domain with large magnitude negative trends in East China while large magnitude positive trends in India subcontinent. AOD trends in India subcontinent demonstrate a relatively more homogeneous spatial pattern than those in East China, with the latter showing a maximum magnitude negative trend (-0.30 decade^{-1}) in the Sichuan Basin. These spatial features of AOD trends in East China and the Indian subcontinent show little seasonal variation, except that no statistically significant trend is observed in summertime in the Indian subcontinent, which could be attributed to the increasing trend in the Indian summer monsoon rainfall since 2002 (Jin and Wang, 2017). Generally, the AOD trends derived from MODIS are greater than those from MISR, partially due to their different sampling size (i.e., sensor swath width). However, non-significant AOD trends are detected in East China in the MERRA-2 data, albeit trends are consistent in the Indian subcontinent among the three datasets. To examine the potential impact of the variations of large-scale sea surface temperature of the Pacific Ocean on the AOD trends, correlation analysis was performed between Nino 3.4 index and the area-averaged AOD over Eastern China and the Indian subcontinent at annual timescale during 2000–2019. Results showed that no statistically significant correlation was detected at the 90% confidence level over the two regions in the

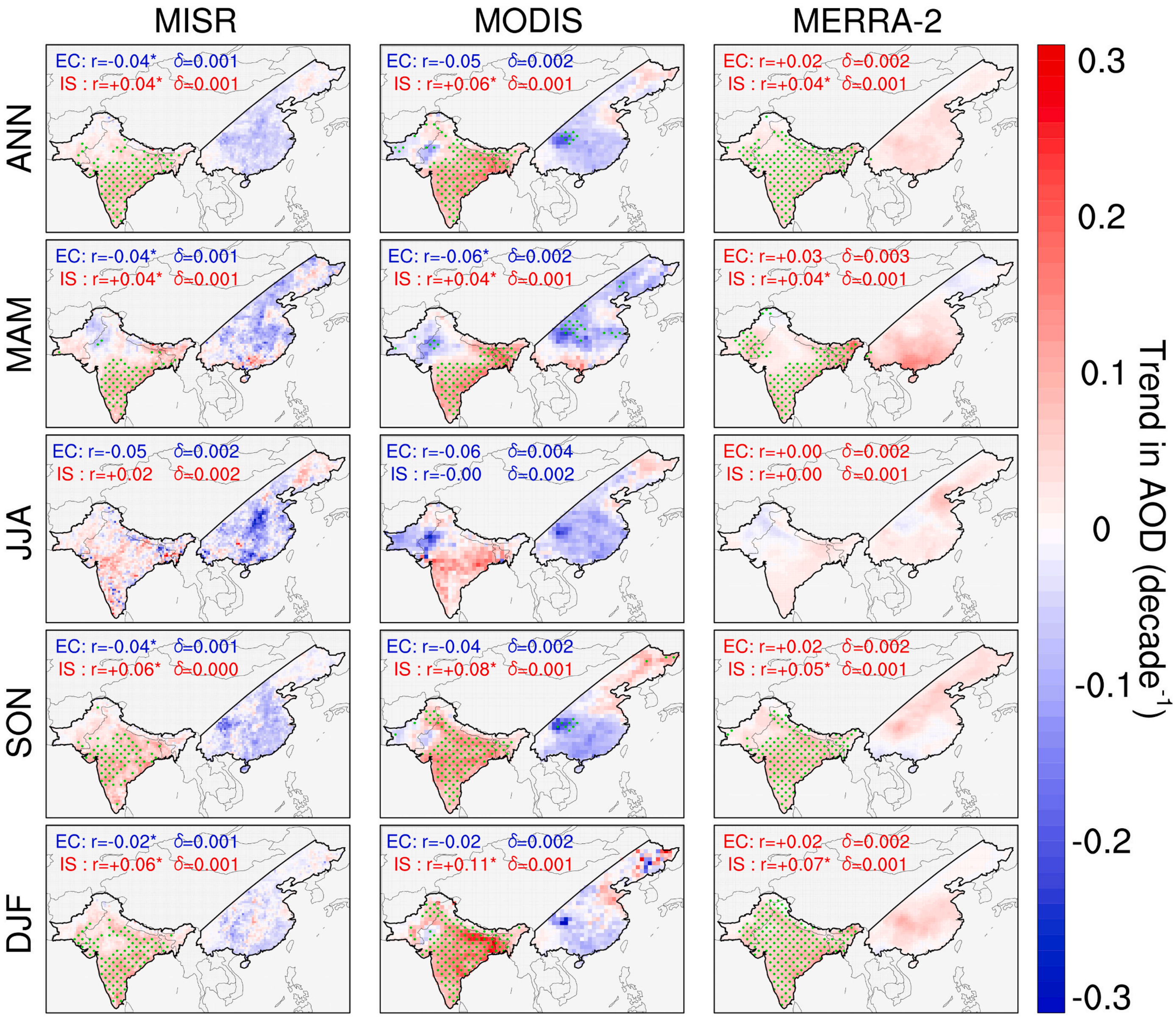

Fig. 4. Annual and seasonal trends in total aerosol optical depth (decade^{-1}) during 2000–2019. The trends are estimated using MERRA-2 data and the least-square regression method. Green dots represent grids with p values small enough to satisfy the FDR criterion $\alpha_{FDR} = 0.10$ [Eq. (1)] so that the statistical significance of the global/field test is at 95% confidence level. The numbers in each panel represent the trends of area-averaged AOD and the corresponding standard deviation. Statistically significant trends at the 90% confident level of aera-average field are marked with a star. (For interpretation of the references to colour in this figure legend, the reader is referred to the web version of this article.)

three AOD datasets.

The area-averaged AOD manifests distinctive decadal variations of AOD over East China and the Indian subcontinent, as shown in Fig. 5. In East China, AOD from MISR, MODIS and MERRA-2 has increased during 2000–2010 but decreased during 2011–2019; such changes in AOD trends from increasing to decreasing appear in all seasons. However, in the Indian subcontinent, the total AOD shows increasing trends from 2000 to 2019 with the fastest increasing trends in SON and DJF.

To address and compare the AOD interdecadal variability in these two regions, trends are further estimated in East China during the former (2000–2010) and latter (2011–2019) periods, and in the Indian subcontinent during the whole period (2000–2019). The breakpoint of 2010 is determined using the piecewise trend detection method introduced in Section 3.3. When applying this method in the area-averaged seasonal AOD time series over East China (Fig. 5), we find different breakpoints. For example, the breakpoints from MERRA-2 are 2010.4, 2011.7, 2007.0, and 2012.5 in the order of spring, summer, fall, and winter. We average the seasonal breakpoints across MERRA-2, MODIS, and MISR datasets and get a single breakpoint of 2010. Therefore, the breakpoint at 2010 for the AOD trend estimation is used for East China (2000–2010 and 2011–2019). From now on, we will focus on only the annual time series, because no consistant breakpoint is detected across seasons. In the Indian subcontinent, the AOD time serieses generally demonstrate persistent increasing trend during the entire period and thus no change point is detected, so our analysis in this region is performed for the entire period.

Fig. 6 illustrates the spatial distribution of AOD trends in East China during the two periods, using the MODIS retrievals and MERRA-2 reanalysis. The trends are estimated using linear regression method based on monthly datasets. Also, the grids with significant trends at the 95% confidence level are marked by green dots. Consistent positive AOD trends are estimated with area-averaged values of +0.11 (MODIS) and + 0.18 decade^{-1} (MERRA-2) in East China. However, during the latter period, the AOD trends in East China turn to negative values ranging from −0.26 (MODIS) to −0.15 decade^{-1} (MERRA-2). During the whole period, AOD trends in the Indian subcontinent are estimated with positive area-averaged values of +0.06 (MODIS) and + 0.04 decade^{-1} (MERRA-2) (Fig. 5). Also, trends estimated using MISR AOD (Fig. S3) have generally consistent patterns with MODIS and MERRA-2 datasets but with smaller magnitudes and fewer grid points that pass the significant test, which can be partially attributed to smaller AOD magnitudes (Fig. 2) and lower sampling frequency of MISR than MODIS, respectively. Spatial aggregation and temporal averaging of daily AOD can help reduce the AOD uncertainties related to background noise and retrieval algorithms (Levy et al., 2015). Since MODIS AOD have larger spatial coverage than MISR and thus smaller uncertainties, it is reasonable to detect more statistically significant AOD trends from MODIS than from MISR. Overall, MODIS and MERRA-2 manifest relatively consistent AOD trends in terms of both spatial and temporal scales. Therefore, MERRA-2 can be employed to perform further analyses with reasonable fidelity.

To test the robustness of the trends estimated using the linear least-

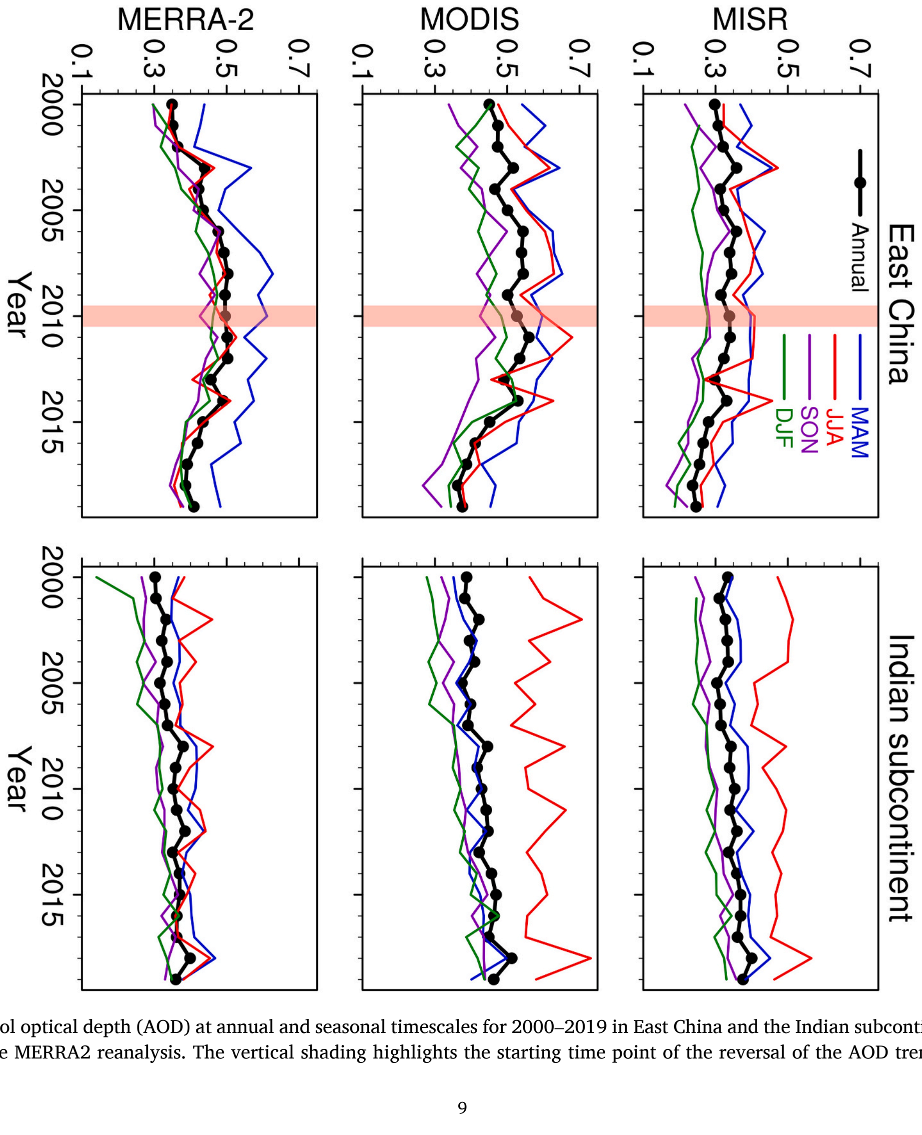

Fig. 5. Time series of aerosol optical depth (AOD) at annual and seasonal timescales for 2000–2019 in East China and the Indian subcontinent. Data are from MODIS and MISR retrievals and the MERRA2 reanalysis. The vertical shading highlights the starting time point of the reversal of the AOD trend in East China.

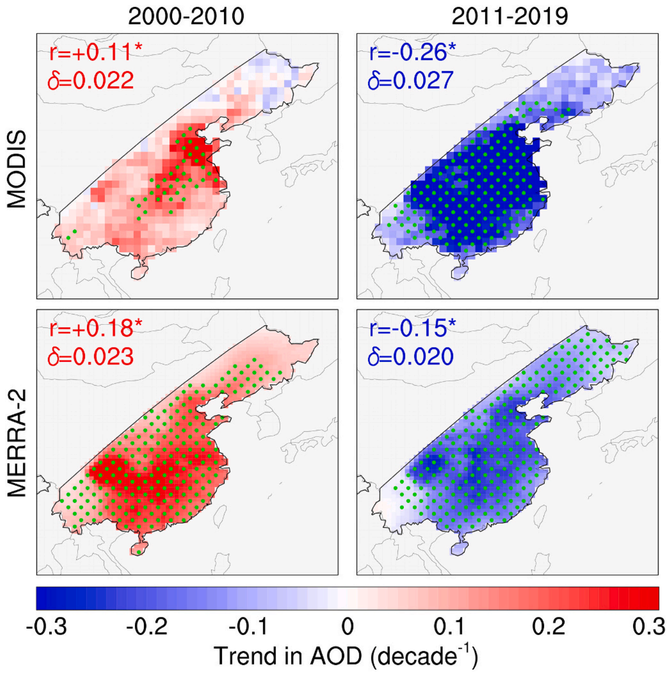

Fig. 6. Spatial patterns of annual and seasonal trends (decade^{-1}) in aerosol optical depth during the two periods of 2000–2010 and 2011–2019 in East China. Data are from MODIS onboard Terra and the MERRA2 reanalysis. Green dots represent grids with p values small enough to satisfy the FDR criterion $\alpha_{FDR} = 0.10$. The numbers in each panel represent the trends of area-averaged AOD and the corresponding standard deviation. Statistically significant trends at the 90% confident level of aera-average field are marked with a star. (For interpretation of the references to colour in this figure legend, the reader is referred to the web version of this article.)

squares regression method in Fig. 6, the other two methods (i.e., the Theil-Sen and bootstrapping) are also applied and the trends are shown in Fig. S4 and S5. Generally, the trends and significance levels estimated by the three methods are consistent in terms of spatial patterns and magnitude.

To attribute the trends in total AOD, AOD trends for individual aerosol species are estimated using the MERRA-2 reanalysis, as shown in Fig. 7 for trends in area-averaged AOD and in Fig.S6 for spatial patterns. In Fig. 7, only statistically significant trends are shown. In East China, the AOD trends during both periods are dominated by the sulfate aerosols, followed by organic carbon aerosols. It is the same with the Indian subcontinent (Fig. S6). Note that the dominant contribution of sulfate aerosols to the total AOD trends are consistent with the Chinese Air Pollution Action Plan released in 2013, which focused on the reduction of sulfate aerosols.

4.3. Trend in the APEEs

4.3.1. Trend in magnitude and frequency of the APEEs

The APEEs (defined as days with AOD over the local 90th percentile) also show significant trends in terms of their magnitude and frequency. Fig. 8(a) illustrates the spatial distribution of the trends in the magnitude of the APEEs at annual timescale based on the MERRA-2 reanalysis. At annual timescale in East China, APEE AOD demonstrates positive trends during the former period with a spatially homogeneous pattern, while the trends are mainly negative during the latter period with strong spatial heterogeneity: large magnitude negative trends in Northeast China and weak trends in other regions. In the Indian subcontinent, slight positive trends are detected except negative trends in a limited area of northwestern India during the whole period. Generally, the APEE AOD trends have similar spatial distribution to that of all-day AOD trends, but manifest larger magnitude. In East China, the trends in APEE AOD can reach ±0.60 decade^{-1} versus ±0.30 decade^{-1} for all-day AOD. This difference is attributable to the AOD absolute range: the APEE AOD is always much larger than the all-day AOD.

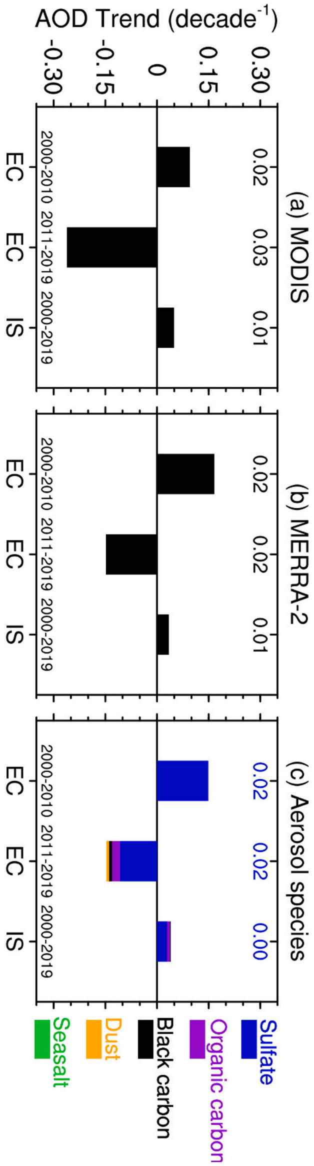

Fig. 7. Annual trends (decade^{-1}) of area-averaged aerosol optical depth (AOD) for total aerosol and aerosol species in East China during two periods of 2000–2010 and 2011–2019 and in the Indian subcontinent during the period of 2000–2019. For aerosol species AOD, only statistically significant trends are shown here.

Fig. 8(b) shows the spatial pattern of the trends in the frequency of the APEEs (i.e., fraction of days with AOD larger than the local 90th percentile in a month) at annual timescale. In East China, more frequent APPEs present in the former period yet less frequent APEEs in the latter period. Relatively larger magnitude frequency trends occur over the southeast China with trends of +6 day month^{-1} decade^{-1} during the former period and −8 day month^{-1} decade^{-1} during the latter period. The area-averaged APPEs frequent are +3.47 day month^{-1} decade^{-1} and –3.58 day month^{-1} decade^{-1} during the two periods. In the Indian subcontinent, positive trends in the APEE frequency are +1.13 day month^{-1} decade^{-1} during the whole period, which are mainly present in South and East India with a magnitude about +3 day month^{-1} decade^{-1}.

(a) APEE AOD

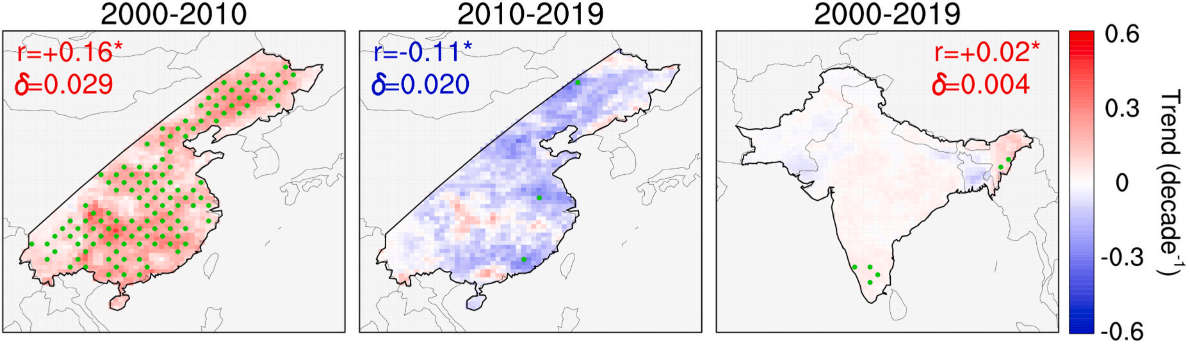

(b) APEE day number

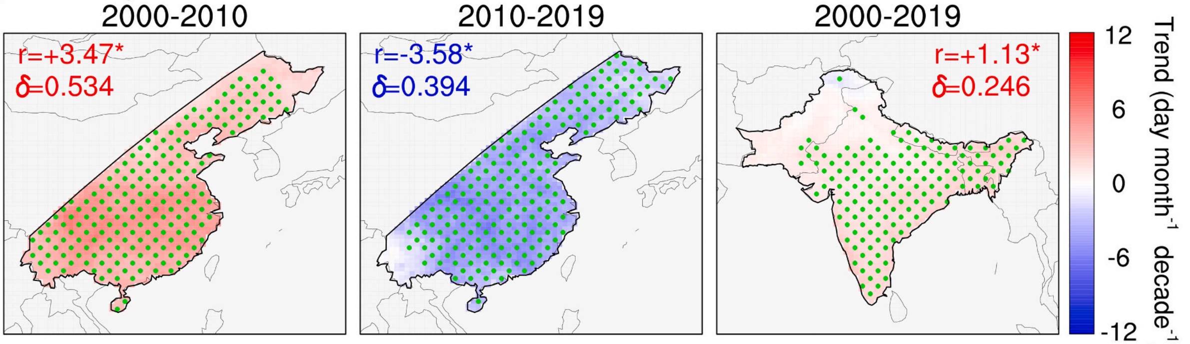

Fig. 8. (a) Annual trends in aerosol optical depth (decade^{-1}) and (b) the frequency (i.e., day number) of the air pollution extreme events (APEEs) for the periods of 2000–2010 (left) and 2011–2019 (middle) in East China and for the period of 2000–2019 (right). Data are from the MERRA2 reanalysis. Green dots represent grids with p values small enough to satisfy the FDR criterion $\alpha_{FDR} = 0.10$. The numbers in each panel represent the trends of area-averaged APEE AOD and the corresponding standard deviation. Statistically significant trends at the 90% confident level of aera-average field are marked with a star. (For interpretation of the references to colour in this figure legend, the reader is referred to the web version of this article.)

4.3.2. *Trend in APEEs magnitude for aerosol species*

To quantify the relative contribution of each aerosol species to the trends in the magnitude of the APEEs, we further calculate AOD trends for sulfate, OC, BC, dust and sea-salt during the APEEs using the MERRA-2 reanalysis, as shown in Fig. 9. In East China, sulfate aerosols demonstrate the largest magnitude of an increasing trend (+0.20 decade^{-1}) during the APEEs in the former period, followed by a decreasing trend of dust (−0.03 decade^{-1}). However, during the latter period, aerosol species demonstrate non-significant trends over most areas in East China. In the Indian subcontinent, sulfate aerosols show the strongest increasing trend (+0.05 decade^{-1}), followed by a decreasing trend of dust (−0.03 decade^{-1}) and an increasing trend of OC (+0.02 decade^{-1}) during the whole period. Large sulfate AOD trends are mainly attributed to the increasing of anthropogenic emission from the rapid development of industrialization and urbanization (e.g., An et al., 2019). The negative trends of dust AOD in the Indian subcontinent is attributed largely to the revival of the Indian summer monsoon and the consequent greening of the Thar Desert from 2002 to 2016 (Jin and Wang, 2017, 2018). For sea salt, the negative trends in the Indian subcontinent can be also caused by the enhanced monsoonal precipitation.

4.3.3. *Trends in area-averaged AOD during the APEEs*

The trends in area-averaged magnitude and frequency of the APEEs over East China and the Indian subcontinent are shown in Fig. 10. The decomposed AOD trends across aerosol species are also analyzed. During the former period in East China, the APEE AOD has increased with an annual rate of +0.16 decade^{-1}; such increases are attributable to sulfate aerosols. During the latter period, the APEE AOD reversed to negative trends in East China due to decrease in sulfate aerosols, with a decreasing trend of −0.12 decade^{-1}. In the Indian subcontinent, the APEE AOD has increased during the whole period, which are mainly caused by sulfate, organic carbon, and dust aerosols. Note that the area-averaged trend of sulfate is positive value of 0.036 decade^{-1} and the trend of dust is negative value of −0.024 decade^{-1}.

For the frequency of the APEEs in East China, it shows positive trends during the former period with a value of about +3.5 day month^{-1} decade^{-1} yet negative trends during the latter period with a value of −3.8 day month^{-1} decade^{-1}. In the Indian subcontinent, the frequency shows positive trends during the former period with a value of +1.1 day month^{-1} decade^{-1}. Generally, East China has experienced more rapid changes in the magnitude and frequency of the APEEs than the Indian subcontinent and these changes are dominated by sulfate aerosols in both regions, but the Indian subcontinent are more susceptible to dust aerosols than East China.

4.4. *Radiation response to AOD trends*

Aerosols can modify the atmospheric heating profile through absorbing and scattering solar radiation, so the changes of AOD could inevitably lead to changes of radiative fluxes. To demonstrate the radiation response to the AOD trends, the trends of shortwave radiation at the surface, in the atmosphere, and at the top of the atmosphere (TOA) are estimated during the former period and the latter period by using CERES and MERRA-2 datasets (Fig. 11 and S7). Comparing to CERES, MERRA-2 can generally well capture the trends of radiation under clear sky condition but exhibit significant discrepancies under all-sky conditions, which is mainly attributed to clouds.

At the surface in East China, annual shortwave radiation shows negative trends during the former period with the area-averaged trends of −3.2 (CERES) and − 4.9 W m^{-2} decade^{-1} (MERRA-2) yet positive trends during the latter period with trends of +7.1 (CERES) and + 5.1 W m^{-2} decade^{-1} (MERRA-2). In the Indian subcontinent, annual

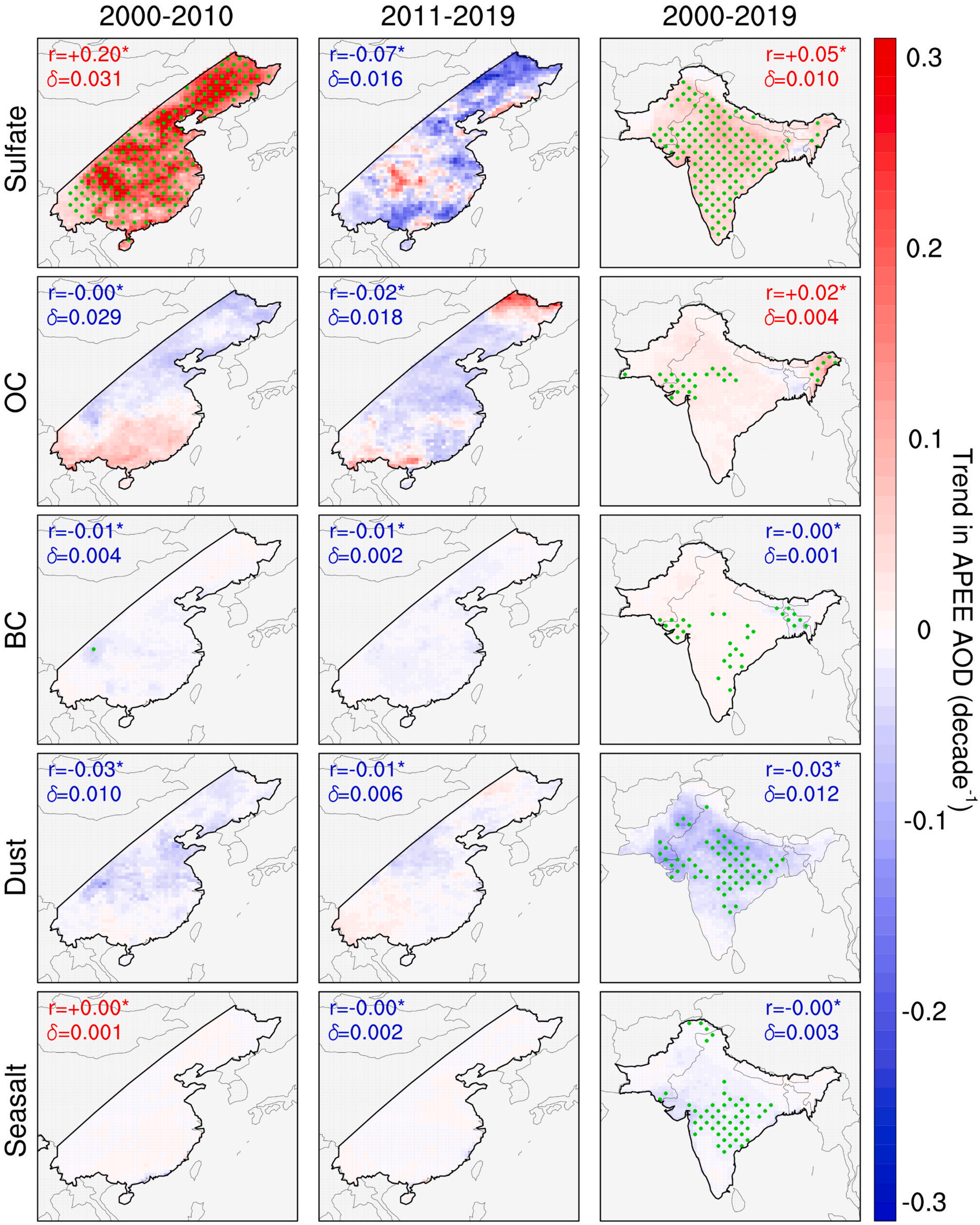

Fig. 9. Annual trends in aerosol optical depth during the aerosol pollution extreme events (APEEs) for sulfate, organic carbon (OC), black carbon (BC), dust and sea-salt during 2000–2010 (left) and 2011–2019 (middle) in East China and during 2000–2019 (right) in the Indian subcontinent. The trends are estimated using the MERRA-2 data and the least-square regression method. Green dots represent grids with p values small enough to satisfy the FDR criterion $\alpha_{FDR} = 0.10$. The numbers in each panel represent the trends of area-averaged APEE AOD and the corresponding standard deviation. Statistically significant trends at the 90% confident level of aera-average field are marked with a star. (For interpretation of the references to colour in this figure legend, the reader is referred to the web version of this article.)

shortwave radiation also demonstrates negative values during the whole period with area-averaged trends of −1.4 (CERES) and − 2.0 W m^{-2} decade^{-1} (MERRA-2).

In the atmosphere in East China, shortwave radiation demonstrates positive trends with an area-averaged value of +1.4 W m^{-2} decade^{-1} (CERES) and +1.1 W m^{-2} decade^{-1} (MERRA-2) during the former period; however, during the latter period, the trends become negative with values of −4.3 (CERES) and −1.6 W m^{-2} decade^{-1} (MERRA-2). In the Indian subcontinent, positive trends are observed during the whole period with the area-averaged trends of +1.7 (CERES) and +1.2

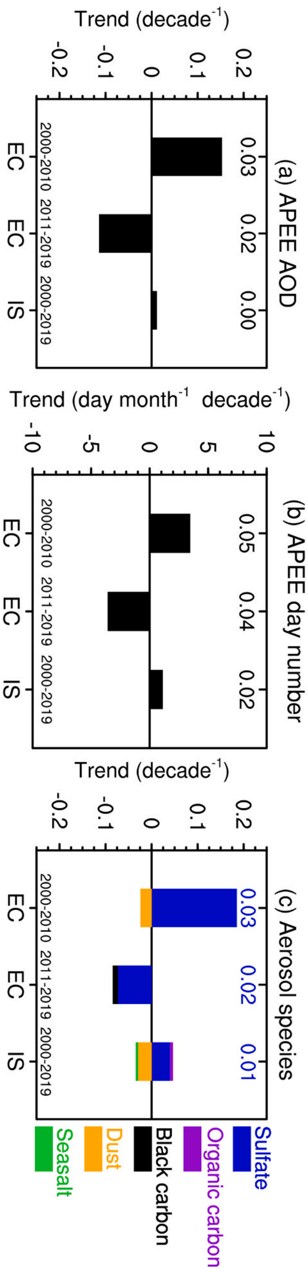

Fig. 10. Annual trends of area-averaged aerosol optical depth (AOD; units: decade^{-1}) for total aerosols (a), day numbers (day month^{-1} decade^{-1}) (b), and aerosol species (c), during the air pollution extreme events (APEEs) in East China for the two periods of 2000–2010 and 2011–2019, and in the Indian suncontinent for the period of 2000–2019. For AOD trends of aerosol species, only statistically significant trends at 95% confidence level are shown.

(MERRA-2) W m^{-2} decade^{-1}.

At TOA in East China, annual shortwave radiation shows significant negative trends with area-averaged values of −1.8 (CERES) and − 4.0 W m^{-2} decade^{-1} (MERRA-2) during the former period, which is consistent with the increases in scattering sulfate aerosol (Fig. 5); however during the latter period, the trends change into positive values of +2.8 (CERES) and + 3.3 W m^{-2} decade^{-1} (MERRA-2). In the Indian subcontinent, a positive trend of +0.5 W m^{-2} decade^{-1} are estimated in CERES versus a negative trend of −0.8 W m^{-2} decade^{-1} in MERRA-2.

Radiation trends at clear-sky conditions reflect only the aerosol–radiation interaction, while the trends at all-sky conditions (Fig. 12) are results of both aerosol–radiation and aerosol–cloud interactions and thus can provide a complete picture of the aerosol–climate interaction. The radiation trends at clear-sky and all-sky conditions are generally similar in CERES in MERRA-2, while important discrepancies are noticeable in some areas due to clouds. For CERES, statistically significant positive trends are detected in the atmosphere over the North China Plain during the first period, which can be attributed to clouds—the increasing low clouds (Fig. 13) can reflect more solar radiation to the aerosol layer above low clouds while the decreasing high clouds can increase the solar radiation that reach the aerosol layer below high clouds, both of which can strengthen the aerosol's warming effect in the atmosphere. No statistically significant trend from CERES is observed at the surface or the top of the atmosphere over the two regions, suggesting that clouds dominate the variations of radiation over these two regions. However, the area-averaged radiation from CERES over East China at the surface demonstrates a significant trend of −4.8 W m^{-2} decade^{-1}, which is due to the reduced uncertainty of AOD when it is spatially averaged. For MERRA-2, negative radiation trends are detected during the latter period at the surface and TOA over some areas in the southern part of East China, which is attributed to increasing clouds (Fig. 13). Moreover, much stronger negative radiation trends are shown over the western and southern Indian subcontinent, which is consistent with the increasing clouds over these regions.

5. Conclusions and discussion

This study examined and compared the long-term trends of AOD, the magnitude and frequency of the APEEs (i.e., daily AOD over the local 90th percentile) from 2000 to 2019 in East China and the Indian subcontinent using multiple satellite retrievals and MERRA-2 aerosol reanalysis. The AOD products from MERRA-2 are evaluated using the satellite retrievals from MODIS and MISR. Generally, MODIS shows a higher AOD than MISR and MERRA-2 over the major desert regions and their downwind regions as well as anthropogenic polluted regions. Relatively, MERRA-2 AOD are more consistent with MISR than with MODIS retrievals. Also, the AOD from the three datasets show similar seasonal variabilities over Asia with peak values in summer and spring over the major study domain. Specifically, high AOD appears in East China and North India in summer. Regarding aerosol species, sulfate AOD dominates over East China and North India with a peak value of 0.6 and 0.4, respectively, followed by high organic and black carbon.

MISR and MODIS exhibit consistent negative-positive northeast-southwest difference in AOD trends from 2000 to 2019, with large magnitude negative trends in East China while large magnitude positive trends in the India subcontinent. Further analysis of the area-averaged AOD timeseries demonstrates distinctive features in the interdecadal variations of AOD over East China and the Indian subcontinent. AOD in East China shows an increasing trend (+0.11 decade^{-1}) during 2000–2010 yet a decreasing trend (−0.26 decade^{-1}) during 2011–2019, forming a reverse V-shape. The decreasing trend can be largely attributed to a more stringent regulations on air pollutant emissions—the Action Plan for the Prevention and Control of Air Pollution—that was issued by the Chinese government in September 2013. On the other hand, AOD in the India subcontinent shows an increasing trend (+0.04 decade^{-1}) over the entire period (2000–2019). This result is different from a previous study, in which an increase in AOD across India from 2010 to 2018 was addressed (Samset et al., 2019). Note that no statistical test was performed on such an increase in AOD (Samset et al., 2019). This difference implies that estimation of long-term changes in AOD without any statistical test might be biased and thus should be reevaluated. Our result also suggests that the current environmental policies in the India subcontinent are not sufficient enough to reverse the increasing aerosol pollution trend.

The magnitude and frequency of the APEE also show significant trends. For the magnitude, a positive trends (+0.16 decade^{-1}) in the APEE AOD is detected from 2000 to 2010 in East China; in contrast, a negative trend (−0.11 decade^{-1}) is observed from 2011 to 2019. In the Indian subcontinent, weak positive trends (+0.02 decade^{-1}) are seen

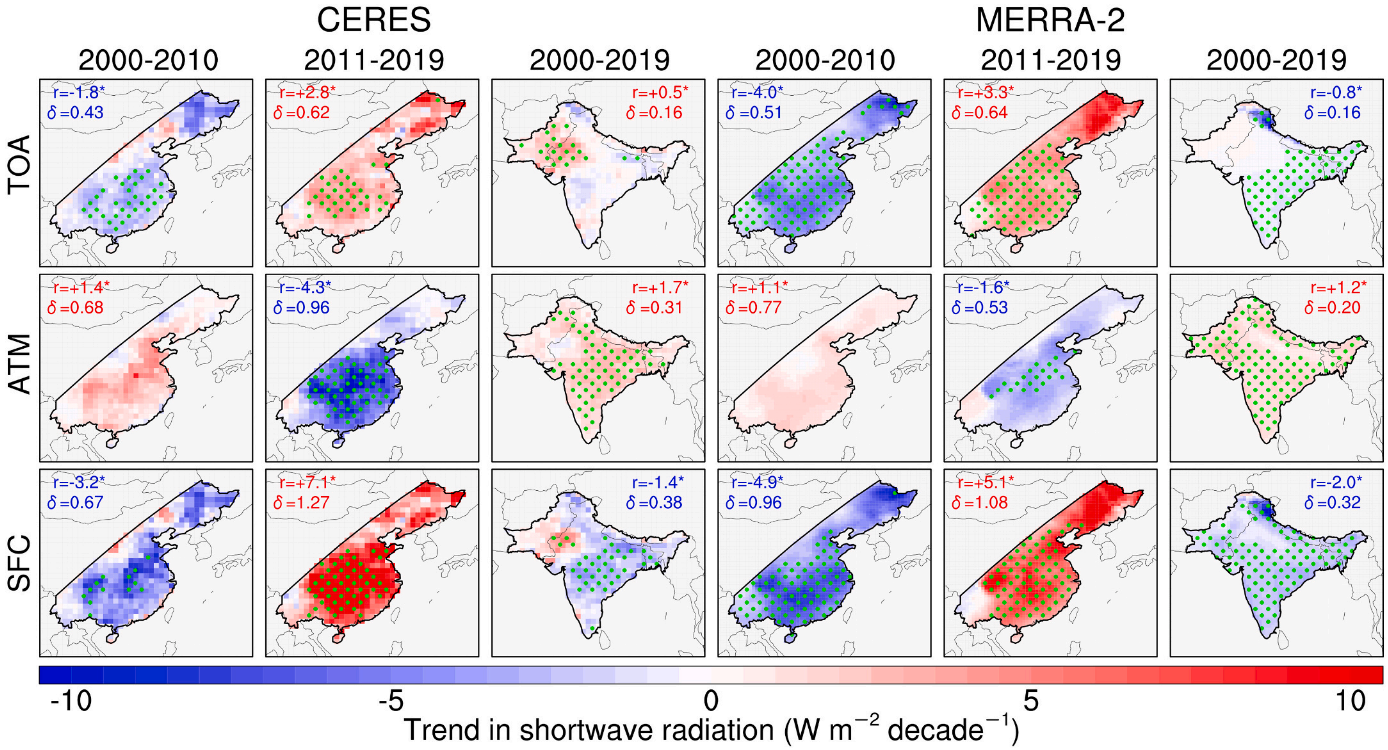

Fig. 11. Spatial patterns of trends in annual clear-sky shortwave radiation (W m^{-2} decade^{-1}) at the top of the atmosphere (TOA), in the atmosphere (ATM), and at the surface (SFC) during periods of 2000–2010 and 2011–2019 in East China and during the period of 2000–2019 in the Indian subcontinent. Data are from CERES and the MERRA-2 reanalysis. Green dots represent grids with p values small enough to satisfy the FDR criterion $\alpha_{FDR} = 0.10$. The numbers in each panel represent the trends of area-averaged radiation and the corresponding standard deviation. Statistically significant trends at the 90% confident level of aera-average field are marked with a star. (For interpretation of the references to colour in this figure legend, the reader is referred to the web version of this article.)

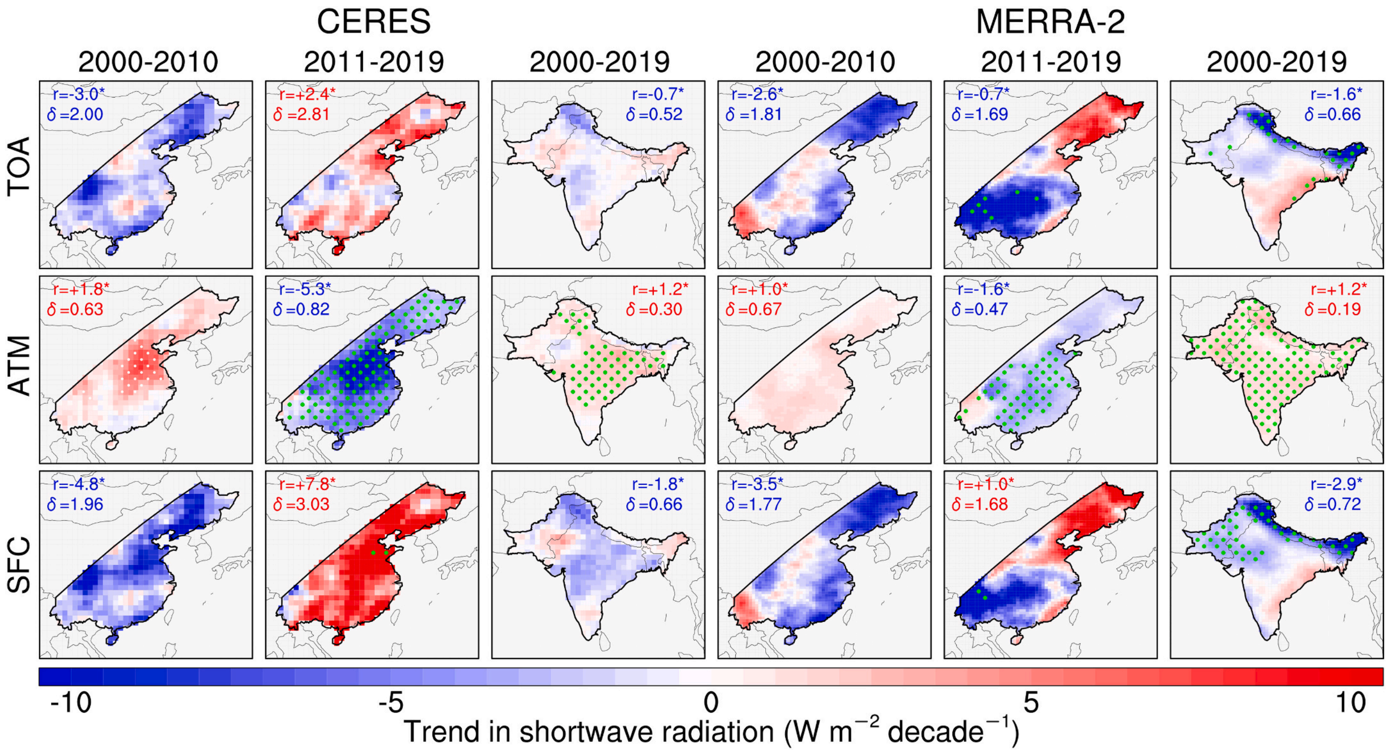

Fig. 12. The same as Fig. 11, but under all-sky condition.

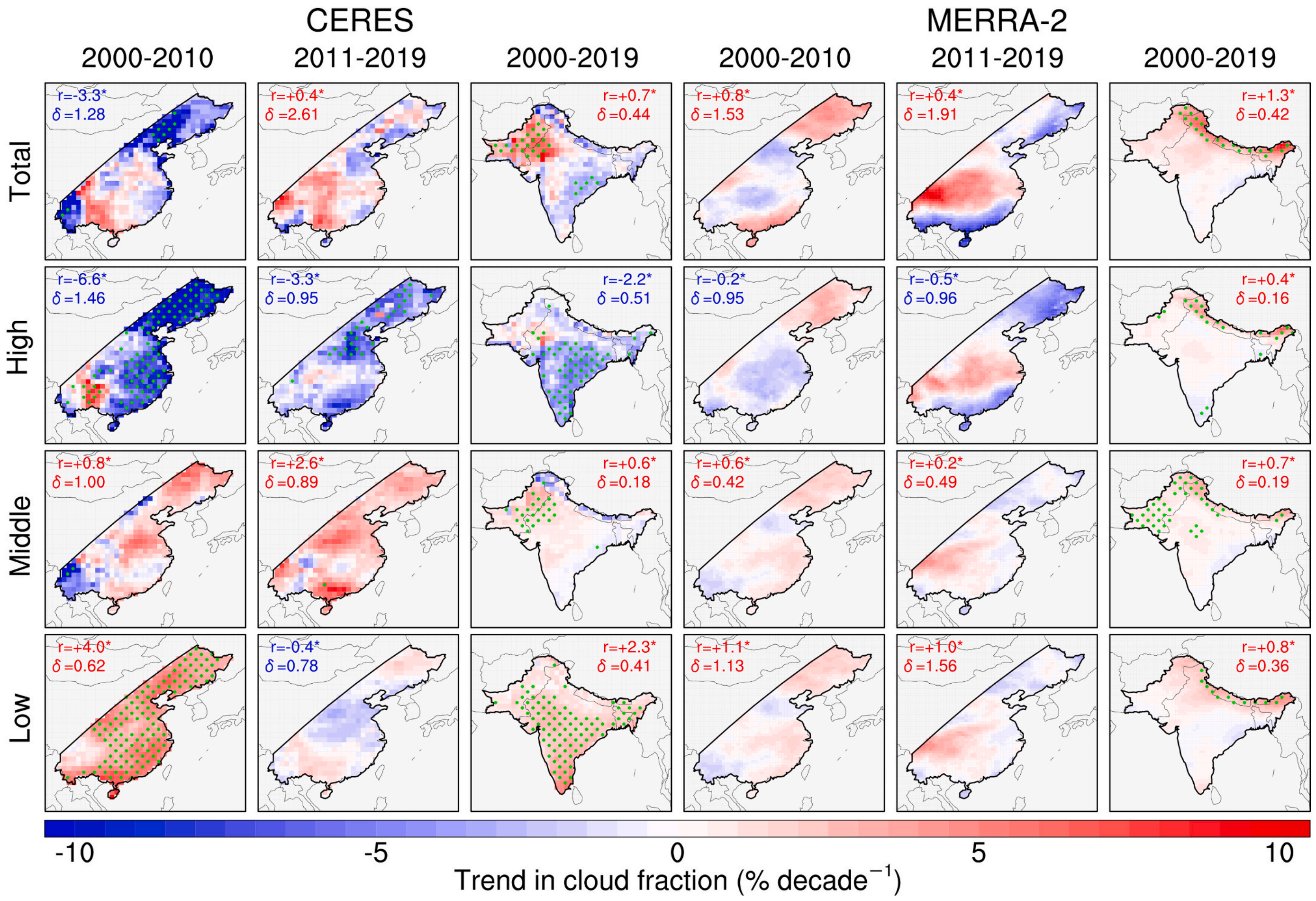

Fig. 13. Spatial patterns of trends in annual cloud cover (% decade^{-1}) for total, high, middle, and low clouds during periods of 2000–2010 and 2011–2019 in East China and during the period of 2000–2019 in the Indian subcontinent. Data are from CERES and the MERRA-2 reanalysis. Green dots represent grids with p values small enough to satisfy the FDR criterion $\alpha_{FDR} = 0.10$. The numbers in each panel represent the trends of area-averaged cloud covers and the corresponding standard deviation. Statistically significant trends at the 90% confident level of aera-average field are marked with a star. (For interpretation of the references to colour in this figure legend, the reader is referred to the web version of this article.)

from 2000 to 2019. For the frequency, more APEEs occurred in East China (+3.47 day month^{-1} decade^{-1}) from 2000 to 2010, while less APEEs days occurred (−3.58 day month^{-1} decade^{-1}) from 2011 to 2019. In the Indian subcontinent, the trend in the APEE frequency is +1.13 day month^{-1} decade^{-1} during the whole period. The trends in the magnitude and frequency of the APEEs show consistent spatial patterns to but greater magnitudes than the trends in the all-day AOD in East China, indicating that the APEEs make a substantial contribution to the all-day AOD trends.

Various aerosol species also demonstrate significant APEE AOD trends. In East China, the positive trends in the APEE AOD from 2000 to 2010 are mainly attributed to sulfate aerosols with an area-averaged value of +0.20 decade^{-1}, while the negative trends for the period of 2011–2019 are attributed to both sulfate and organic aerosols. In the India subcontinent, the positive trends in APEE AOD during the entire period are mainly caused by the sulfate aerosols with a value of +0.05 decade^{-1}, followed by the dust (−0.03 decade^{-1}) and OC (+0.02 decade^{-1}).

Associated with AOD trends, clear-sky radiation from CERES and MERRA-2 shows significant trends over the study domain. In East China, clear-sky shortwave radiation shows negative trends (−3.2 W m^{-2} decade^{-1}) at the surface yet positive trends (+1.4 W m^{-2} decade^{-1}) in the atmosphere from 2000 to 2010; these trends reversed during the period of 2011–2019. In the India subcontinent, clear-sky shortwave radiation shows negative trends (−1.4 W m^{-2} decade^{-1}) at the surface from 2000 to 2019. On the other hand, all-sky radiation exhibits consistent trends to clear-sky radiation in the atmosphere but large discrepancies at the surface and TOA in both CERES and MERRA-2, suggesting that absorbing aerosols dominate the radiation budget in the atmosphere over East China and the Indian subcontinent. Moreover, the discrepancies of radiation trends between clear-sky and all-sky conditions are larger in MERRA-2 than in CERES even though the former demonstrates much weaker trends in clouds, implying that MERRA-2 might overestimate the radiation responses to clouds.

It is noteworthy that there are some caveats in this study. First, the MERRA-2 reanalysis makes it possible, for the first time, to unveil the spatiotemporal features of the air pollution extreme event at the global scale, but it does not simulate nitrate and ammonium aerosols due to high computational cost for associated gas-phase chemistry and aerosol thermodynamics (Liu et al., 2012). Nitrate and ammonium aerosols have been shown to contribute an annual average of 15% to total AOD in East Asia (Park et al., 2014) and play an important role in ice cloud formation and aerosol indirect radiative effect during Asian monsoons (Höpfner et al., 2019). Moreover, the emissions of these two aerosols and their ratios to total aerosols have demonstrated generally increasing trends during the past two or so decades in Asia due to increasing agricultural activities and rapid decrease in sulfate aerosols (Zhao et al., 2017). Therefore, although a lack of these two aerosol species in the MERRA-2 reanalysis does not influence the trend estimation of total AOD since satellite-retrieved AOD are assimilated, it could result in overestimation of AOD trends of other anthropogenic aerosol species (e.g., sulfate or black carbon) as well as radiation trends. Second, although we focused on the period from 2000 to 2019 when Terra satellite has continuous observations, the estimation of long-term trends in AOD using the MERRA-2 reanalysis could be biased by changes in the observing system (McCarty et al., 2016; Randles et al., 2017) and discontinuous MISR and AERONET AOD data assimilated in the reanalysis (see Section 2.3). To what extent the changes in the assimilation sources of AOD affect the accuracy of AOD trend is still an open question. Third, the AOD trend estimation could be biased by the long-term drift of Terra-MODIS deepblue AOD, which is restricted to 0.005 ± 0.002 (trend and one standard deviation) per decade (Sayer et al., 2019). However, the AOD trends discussed here ranges from 0.06 to 0.4 per decade, so such a small AOD drift should not be a serious issue in this study but could play a role in AOD trend estimation in regions with more gradual changes in aerosol concentrations than in East China and the Indian subcontinent. Last, it should be pointed out that although this paper is focused on trends that are statistically significant (i.e., trends large with low uncertainties), their counterparts—insignificant trends (i.e., trends small with low uncertainties or trends large with high uncertainties)—also have important implications, in particular from the perspective of policy makers. The first means that any trend is likely small so we don't need to worry about it while the second means that we don't know whether the trend is large or small because its uncertianty is high, so we need to improve the monitoring techniques and/or prepare to deal with a potential large trend. The distinction between these two types of insignificant trends are out the scope of this paper.

In summary, our results show that the air quality has been improving in East China during the past decade but not in the Indian subcontinent. To combat with the severe air pollution issues, the Indian government has initialized a National Clean Air Program in January 2019 (Sundaray and Bhardwaj, 2019), with an aim to significantly reduce particle pollutant concentrations by 20–30% by 2024 and even more in a long-term plan in 20–25 years. Therefore, it is important to use new satellite platforms after Terra mission that will end around 2026 to continuously monitor the aerosol pollution in the Indian subcontinent and other regions in Asia and address the associated economic and climatic impacts. Unfortunately, we will face a gap because there is no planned U.S. satellite platform that has an equator crossing time of 10:30 a.m. local time. However, there are some potential satellite candidates that could be used to extend the Terra's mission in regard to aerosol observations. For example, the Suomi National Polar-orbiting Partnership (S-NPP) satellite and the NASA-NOAA Joint Polar Satellite System (JPSS) with equator crossing time of 1:30 p.m. local time have been planned to last through 2031 (Hsu et al., 2019). The Visible Infrared Imaging Radiometer Suite (VIIRS) onboard these satellites have very similar spectral bands to and higher spatial resolution than Terra-MODIS. Moreover, the MODIS aerosol retrieval algorithms have been already applied in VIIRS and demonstrated a good consistency (Hsu et al., 2019). All of these similarities make VIIRS a good if not a perfect successor of Terra-MODIS given another fact that the morning–afternoon offset (~0.01) between Terra-MODIS and Aqua-MODIS AOD is attributed to sensor calibration or retrieval artefact instead of a temporal component of the aerosol system (Remer et al., 2020) and could be removed in the future (Levy et al., 2013). Besides polar-orbiting satellites, the fusion of multiple geostationary satellites from different space agencies could provide another opportunity to extend Terra's record of global aerosol observations but with hourly resolution (Xie et al., 2020). With an increasing number of satellites in orbits, it is of substantial importance to develop a consistent aerosol retrieval algorithm and apply it to various sensors with similar configuration so that a long-term and consistent dataset of aerosols will be available to the climate and environmental communities in the future.

Declaration of Competing Interest

The authors declare that they have no known competing financial interests or personal relationships that could have appeared to influence the work reported in this paper.

Acknowledgements

This research was supported by the Foundation for National Natural Science Foundation of China (No. 91644225, No. 41805116, and No. 42075105). Y. Y. Ma was also funded by the National Nature Science Foundation of China (No. 41905013) and the CAS “Light of West China” Program. Z. M. Ji was also funded by the Open Program (SKLCS-OP-2020-9) from State Key Laboratory of Cryospheric Science, Northwest Institute of Eco-Environment and Resources, Chinese Academy of Sciences, and the Joint Open Project of KLME and CIC-FEMD (grant KLME201901).

Appendix A. Supplementary data

Supplementary data to this article can be found online at https://doi.org/10.1016/j.rse.2021.112541.

References

Alpert, P., 2012. AOD trends over megacities based on space monitoring using MODIS and MISR. Am. J. Clim. Chang. 01, 117–131.

An, Z.S., Huang, R.J., Zhang, R.Y., Tie, X.X., Li, G.H., Cao, J.J., Zhou, W.J., Shi, Z.G., Han, Y.M., Gu, Z.L., Ji, Y.M., 2019. Severe haze in northern China: a synergy of anthropogenic emissions and atmospheric processes. Proc. Natl. Acad. Sci. U. S. A. 116, 8657–8666.

Balakrishnan, K., Dey, S., Gupta, T., Dhaliwal, R.S., Brauer, M., Cohen, A.J., Stanaway, J.D., Beig, G., Joshi, T.K., Aggarwal, A.N., Sabde, Y., Sadhu, H., Frostad, J., Causey, K., Godwin, W., Shukla, D.K., Kumar, G.A., Varghese, C.M., Muraleedharan, P., Agrawal, A., Anjana, R.M., Bhansali, A., Bhardwaj, D., Burkart, K., Cercy, K., Chakma, J.K., Chowdhury, S., Christopher, D.J., Dutta, E., Furtado, M., Ghosh, S., Ghoshal, A.G., Glenn, S.D., Guleria, R., Gupta, R., Jeemon, P., Kant, R., Kant, S., Kaur, T., Koul, P.A., Krish, V., Krishna, B., Larson, S.L., Madhipatla, K., Mahesh, P.A., Mohan, V., Mukhopadhyay, S., Mutreja, P., Naik, N., Nair, S., Nguyen, G., Odell, C.M., Pandian, J.D., Prabhakaran, D., Prabhakaran, P., Roy, A., Salvi, S., Sambandam, S., Saraf, D., Sharma, M., Shrivastava, A., Singh, V., Tandon, N., Thomas, N.J., Torre, A., Xavier, D., Yadav, G., Singh, S., Shekhar, C., Vos, T., Dandona, R., Reddy, K.S., Lim, S.S., Murray, C.J.L., Venkatesh, S., Dandona, L., 2019. The impact of air pollution on deaths, disease burden, and life expectancy across the states of India: the global burden of disease study 2017. The Lancet Planetary Health 3, e26–e39.

Benjamini, Y., Hochberg, Y., 1995. Controlling the false discovery rate - a practical and powerful approach to multiple testing. J. Royal Stat. Soc. Series B-Methodol. 57, 289–300.

Burnett, R., Chen, H., Szyszkowicz, M., Fann, N., Hubbell, B., Pope 3rd, C.A., Apte, J.S., Brauer, M., Cohen, A., Weichenthal, S., Coggins, J., Di, Q., Brunekreef, B., Frostad, J., Lim, S.S., Kan, H., Walker, K.D., Thurston, G.D., Hayes, R.B., Lim, C.C., Turner, M.C., Jerrett, M., Krewski, D., Gapstur, S.M., Diver, W.R., Ostro, B., Goldberg, D., Crouse, D.L., Martin, R.V., Peters, P., Pinault, L., Tjepkema, M., van Donkelaar, A., Villeneuve, P.J., Miller, A.B., Yin, P., Zhou, M., Wang, L., Janssen, N.A.H., Marra, M., Atkinson, R.W., Tsang, H., Quoc Thach, T., Cannon, J.B., Allen, R.T., Hart, J.E., Laden, F., Cesaroni, G., Forastiere, F., Weinmayr, G., Jaensch, A., Nagel, G., Concin, H., Spadaro, J.V., 2018. Global estimates of mortality associated with long-term exposure to outdoor fine particulate matter. Proc. Natl. Acad. Sci. U. S. A. 115, 9592–9597.

Che, H., Gui, K., Xia, X., Wang, Y., Holben, B.N., Goloub, P., Cuevas-Agulló, E., Wang, H., Zheng, Y., Zhao, H., Zhang, X., 2019. Large contribution of meteorological factors to inter-decadal changes in regional aerosol optical depth. Atmos. Chem. Phys. 19, 10497–10523.

de Meij, A., Pozzer, A., Lelieveld, J., 2012. Trend analysis in aerosol optical depths and pollutant emission estimates between 2000 and 2009. Atmos. Environ. 51, 75–85.

Di, Q., Kloog, I., Koutrakis, P., Lyapustin, A., Wang, Y.J., Schwartz, J., 2016. Assessing PM2.5 exposures with high spatiotemporal resolution across the continental United States. Environ. Sci. Technol. 50, 4712–4721.

Di, Q., Wang, Y., Zanobetti, A., Wang, Y., Koutrakis, P., Choirat, C., Dominici, F., Schwartz, J.D., 2017. Air pollution and mortality in the Medicare population. N. Engl. J. Med. 376, 2513–2522.

Diner, D.J., Beckert, J.C., Reilly, T.H., Bruegge, C.J., Conel, J.E., Kahn, R.A., Martonchik, J.V., Ackerman, T.P., Davies, R., Gerstl, S.A.W., Gordon, H.R., Muller, J.P., Myneni, R.B., Sellers, P.J., Pinty, B., Verstraete, M.M., 1998. Multi-angle imaging SpectroRadiometer (MISR) - instrument description and experiment overview. IEEE Trans. Geosci. Remote Sens. 36, 1072–1087.

Fan, J.W., Wang, Y., Rosenfeld, D., Liu, X.H., 2016. Review of aerosol-cloud interactions: mechanisms, significance, and challenges. J. Atmos. Sci. 73, 4221–4252.

Fan, H., Zhao, C., Yang, Y., 2020. A comprehensive analysis of the spatio-temporal variation of urban air pollution in China during 2014–2018. Atmos. Environ. 220.

Fernandes, R., Leblanc, S.G., 2005. Parametric (modified least squares) and non-parametric (Theil-Sen) linear regressions for predicting biophysical parameters in the presence of measurement errors. Remote Sens. Environ. 95, 303–316.

Fu, Q., Liou, K.N., 1993. Parameterization of the radiative properties of cirrus clouds. J. Atmos. Sci. 50, 2008–2025.

Garay, M.J., Witek, M.L., Kahn, R.A., Seidel, F.C., Limbacher, J.A., Bull, M.A., Diner, D. J., Hansen, E.G., Kalashnikova, O.V., Lee, H., Nastan, A.M., Yu, Y., 2020. Introducing the 4.4 km spatial resolution multi-angle imaging SpectroRadiometer (MISR) aerosol product. Atmos. Measur. Techn. 13, 593–628.

Gelaro, R., McCarty, W., Suarez, M.J., Todling, R., Molod, A., Takacs, L., Randles, C.A., Darmenov, A., Bosilovich, M.G., Reichle, R., Wargan, K., Coy, L., Cullather, R., Draper, C., Akella, S., Buchard, V., Conaty, A., da Silva, A.M., Gu, W., Kim, G.K., Koster, R., Lucchesi, R., Merkova, D., Nielsen, J.E., Partyka, G., Pawson, S., Putman, W., Rienecker, M., Schubert, S.D., Sienkiewicz, M., Zhao, B., 2017. The modern-era retrospective analysis for research and applications, version 2 (MERRA-2). J. Clim. 30, 5419–5454.

Goldman, G.T., Dominici, F., 2019. Don't abandon evidence and process on air pollution policy. Science 363, 1398–1440.

Gong, S.L., 2003. A parameterization of sea-salt aerosol source function for sub- and super-micron particles. Glob. Biogeochem. Cycles 17.

Gristey, J.J., Chiu, J.C., Gurney, R.J., Morcrette, C.J., Hill, P.G., Russell, J.E., Brindley, H. E., 2018. Insights into the diurnal cycle of global earth outgoing radiation using a numerical weather prediction model. Atmos. Chem. Phys. 18, 5129–5145.

Guo, J.-P., Zhang, X.-Y., Wu, Y.-R., Zhaxi, Y., Che, H.-Z., La, B., Wang, W., Li, X.-W., 2011. Spatio-temporal variation trends of satellite-based aerosol optical depth in China during 1980–2008. Atmos. Environ. 45, 6802–6811.

Gupta, P., Levy, R.C., Mattoo, S., Remer, L.A., Munchak, L.A., 2016. A surface reflectance scheme for retrieving aerosol optical depth over urban surfaces in MODIS dark target retrieval algorithm. Atmos. Measur. Techn. 9, 3293–3308.

Heidinger, A.K., Cao, C.Y., Sullivan, J.T., 2002. Using Moderate Resolution Imaging Spectrometer (MODIS) to calibrate advanced very high resolution radiometer reflectance channels. J. Geophys. Res.-Atmos. *107*.

Heidinger, A.K., Foster, M.J., Walther, A., Zhao, X.P., 2014. The pathfinder atmospheres-extended Avhrr climate dataset. Bull. Am. Meteorol. Soc. 95, 909.

Holben, B.N., Eck, T.F., Slutsker, I., Tanre, D., Buis, J.P., Setzer, A., Vermote, E., Reagan, J.A., Kaufman, Y.J., Nakajima, T., Lavenu, F., Jankowiak, I., Smirnov, A., 1998. AERONET - a federated instrument network and data archive for aerosol characterization. Remote Sens. Environ. 66, 1–16.

Höpfner, M., Ungermann, J., Borrmann, S., Wagner, R., Spang, R., Riese, M., Stiller, G., Appel, O., Batenburg, A.M., Bucci, S., Cairo, F., Dragoneas, A., Friedl-Vallon, F., Hünig, A., Johansson, S., Krasauskas, L., Legras, B., Leisner, T., Mahnke, C., Möhler, O., Molleker, S., Müller, R., Neubert, T., Orphal, J., Preusse, P., Rex, M., Saathoff, H., Stroh, F., Weigel, R., Wohltmann, I., 2019. Ammonium nitrate particles formed in upper troposphere from ground ammonia sources during Asian monsoons. Nat. Geosci. 12, 608–612.

Hsu, N.C., Herman, J., Torres, O., Holben, B., Tanre, D., Eck, T., Smirnov, A., Chatenet, B., Lavenu, F., 1999. Comparisons of the TOMS aerosol index with Sun-photometer aerosol optical thickness: results and applications. J. Geophys. Res.-Atmos. 104, 6269–6279.

Hsu, N.C., Tsay, S.C., King, M.D., Herman, J.R., 2004. Aerosol properties over bright-reflecting source regions. IEEE Trans. Geosci. Remote Sens. 42, 557–569.

Hsu, N.C., Tsay, S.C., King, M.D., Herman, J.R., 2006. Deep blue retrievals of Asian aerosol properties during ACE-Asia. IEEE Trans. Geosci. Remote Sens. 44, 3180–3195.

Hsu, N.C., Gautam, R., Sayer, A.M., Bettenhausen, C., Li, C., Jeong, M.J., Tsay, S.C., Holben, B.N., 2012. Global and regional trends of aerosol optical depth over land and ocean using SeaWiFS measurements from 1997 to 2010. Atmos. Chem. Phys. 12, 8037–8053.

Hsu, N.C., Jeong, M.J., Bettenhausen, C., Sayer, A.M., Hansell, R., Seftor, C.S., Huang, J., Tsay, S.C., 2013. Enhanced deep blue aerosol retrieval algorithm: the second generation. J. Geophys. Res.-Atmos. 118, 9296–9315.

Hsu, N., Lee, J., Sayer, A., Carletta, N., Chen, S.H., Tucker, C., Holben, B., Tsay, S.C., 2017. Retrieving near-global aerosol loading over land and ocean from AVHRR. J. Geophys. Res.-Atmos. 122, 9968–9989.

Hsu, N., Lee, J., Sayer, A., Kim, W., Bettenhausen, C., Tsay, S.C., 2019. VIIRS deep blue aerosol products over land: extending the EOS long-term aerosol data records. J. Geophys. Res.-Atmos. 124, 4026–4053.

Jaramillo, P., Muller, N.Z., 2016. Air pollution emissions and damages from energy production in the U.S.: 2002–2011. Energy Policy 90, 202–211.

Jethva, H., Chand, D., Torres, O., Gupta, P., Lyapustin, A., Patadia, F., 2018. Agricultural burning and air quality over northern India: a synergistic analysis using NASA's A-train satellite data and ground measurements. Aerosol Air Qual. Res. 18, 1756–1773.

Jin, Q., Pryor, S.C., 2020. Long-term trends of high aerosol pollution events and their climatic impacts in North America using multiple satellite retrievals and modern-era retrospective analysis for research and applications version 2. J. Geophys. Res.-Atmos. 125.

Jin, Q., Wang, C., 2017. A revival of Indian summer monsoon rainfall since 2002. Nat. Clim. Chang. 7, 587–594.

Jin, Q., Wang, C., 2018. The greening of northwest Indian subcontinent and reduction of dust abundance resulting from Indian summer monsoon revival. Sci. Rep. 8.

Jin, Q., Wei, J., Yang, Z.-L., 2014. Positive response of Indian summer rainfall to Middle East dust. Geophys. Res. Lett. 41, 4068–4074.

Jin, Q., Wei, J., Yang, Z.-L., Pu, B., Huang, J., 2015. Consistent response of Indian summer monsoon to Middle East dust in observations and simulations. Atmos. Chem. Phys. 15, 9897–9915.

Jin, Q., Yang, Z.-L., Wei, J., 2016a. High sensitivity of Indian summer monsoon to Middle East dust absorptive properties. Sci. Rep. 6, 30690.

Jin, Q., Yang, Z.-L., Wei, J., 2016b. Seasonal responses of Indian summer monsoon to dust aerosols in the Middle East, India, and China. J. Clim. 29, 632–6349.

Jin, Qinjian, Wei, Jiangfeng, Lau, William K.M., Pu, Bing, Wang, Chien, 2021. Interactions of Asian mineral dust with Indian summer monsoon: Recent advances and challenges. Earth-Science Reviews 215, 103562.

Jin, Q., Wei, J., Pu, B., Yang, Z.L., Parajuli, S.P., 2018. High summertime aerosol loadings over the Arabian Sea and their transport pathways. J. Geophys. Res.-Atmos. 123, 10568–10590.

Jin, Q., Crippa, P., Pryor, S., 2020. Spatial characteristics and temporal evolution of the relationship between PM2. 5 and aerosol optical depth over the eastern USA during 2003–2017. Atmos. Environ. 117718.

Jones, B., O'Neill, B.C., 2016. Spatially explicit global population scenarios consistent with the Shared Socioeconomic Pathways. Environ. Res. Lett. 11.

Kahn, R.A., Gaitley, B.J., Martonchik, J.V., Diner, D.J., Crean, K.A., Holben, B., 2005. Multiangle Imaging Spectroradiometer (MISR) global aerosol optical depth validation based on 2 years of coincident Aerosol Robotic Network (AERONET) observations. J. Geophys. Res.-Atmos. *110*.

Kalashnikova, O.V., Garay, M.J., Martonchik, J.V., Diner, D.J., 2013. MISR dark water aerosol retrievals: operational algorithm sensitivity to particle non-sphericity. Atmos. Measur. Techn. 6, 2131–2154.

Kaskaoutis, D.G., Kharol, S.K., Sinha, P.R., Singh, R.P., Badarinath, K.V.S., Mehdi, W., Sharma, M., 2011. Contrasting aerosol trends over South Asia during the last decade based on MODIS observations. Atmos. Meas. Tech. Discuss. 5275–5323.

Kaufman, Y.J., Tanré, D., Remer, L.A., Vermote, E., Chu, A., Holben, B., 1997. Operational remote sensing of tropospheric aerosol over land from EOS moderate resolution imaging spectroradiometer. J. Geophys. Res.-Atmos. 102, 17051–17067.

Kendall, M.G., 1955. Rank Correlation Methods. Griffin, London.

King, M.D., Kaufman, Y.J., Menzel, W.P., Tanre, D., 1992. Remote sensing of cloud, aerosol, and water vapor properties from the moderate resolution imaging spectrometer(MODIS). IEEE Trans. Geosci. Remote Sens. 30, 2–27.

King, M.D., Kaufman, Y.J., Tanre, D., Nakajima, T., 1999. Remote sensing of tropospheric aerosols from space: past, present, and future. Bull. Am. Meteorol. Soc. 80, 2229–2259.

Kleist, D.T., Parrish, D.F., Derber, J.C., Treadon, R., Wu, W.S., Lord, S., 2009. Introduction of the GSI into the NCEP global data assimilation system. Weather Forecast. 24, 1691–1705.

Klingmüller, K., Pozzer, A., Metzger, S., Stenchikov, G.L., Lelieveld, J., 2016. Aerosol optical depth trend over the Middle East. Atmos. Chem. Phys. 16, 5063–5073.

Kokhanovsky, A.A., Leeuw, G., 2009. Satellite aerosol remote sensing over land. Springer.

Kumar, S., Arora, A., 2018. On the connection between remote dust aerosol and Indian summer monsoon. Theor. Appl. Climatol. 137, 929–940. https://doi.org/10.1007/s00704-018-2647-6.

Lahoz, W.A., Schneider, P., 2014. Data assimilation: making sense of earth observation. Front. Environ. Sci. 2.

Landrigan, P.J., Fuller, R., Acosta, N.J.R., Adeyi, O., Arnold, R., Basu, N., Balde, A.B., Bertollini, R., Bose-O'Reilly, S., Boufford, J.I., Breysse, P.N., Chiles, T., Mahidol, C., Coll-Seck, A.M., Cropper, M.L., Fobil, J., Fuster, V., Greenstone, M., Haines, A., Hanrahan, D., Hunter, D., Khare, M., Krupnick, A., Lanphear, B., Lohani, B., Martin, K., Mathiasen, K.V., McTeer, M.A., Murray, C.J.L., Ndahimananjara, J.D., Perera, F., Potocnik, J., Preker, A.S., Ramesh, J., Rockstrom, J., Salinas, C., Samson, L.D., Sandilya, K., Sly, P.D., Smith, K.R., Steiner, A., Stewart, R.B., Suk, W. A., van Schayck, O.C.P., Yadama, G.N., Yumkella, K., Zhong, M., 2018. The lancet commission on pollution and health. Lancet 391, 462–512.

Lelieveld, J., Evans, J.S., Fnais, M., Giannadaki, D., Pozzer, A., 2015. The contribution of outdoor air pollution sources to premature mortality on a global scale. Nature 525, 367–371.

Lelieveld, J., Klingmuller, K., Pozzer, A., Poschl, U., Fnais, M., Daiber, A., Munzel, T., 2019. Cardiovascular disease burden from ambient air pollution in Europe reassessed using novel hazard ratio functions. Eur. Heart J. 40, 1590–1596.

Levy, R.C., Remer, L.A., Mattoo, S., Vermote, E.F., Kaufman, Y.J., 2007. Second-generation operational algorithm: retrieval of aerosol properties over land from inversion of moderate resolution imaging spectroradiometer spectral reflectance. J. Geophys. Res.-Atmos. 112.

Levy, R.C., Mattoo, S., Munchak, L.A., Remer, L.A., Sayer, A.M., Patadia, F., Hsu, N.C., 2013. The collection 6 MODIS aerosol products over land and ocean. Atmos. Measur. Techn. 6, 2989–3034.

Levy, R.C., Munchak, L.A., Mattoo, S., Patadia, F., Remer, L.A., Holz, R.E., 2015. Towards a long-term global aerosol optical depth record: applying a consistent aerosol retrieval algorithm to MODIS and VIIRS-observed reflectance. Atmos. Measur. Techn. 8, 4083–4110.

Li, J., Jian, B., Huang, J., Hu, Y., Zhao, C., Kawamoto, K., Liao, S., Wu, M., 2018. Long-term variation of cloud droplet number concentrations from space-based Lidar. Remote Sens. Environ. 213, 144–161.

Li, K., Jacob, D.J., Liao, H., Shen, L., Zhang, Q., Bates, K.H., 2019. Anthropogenic drivers of 2013-2017 trends in summer surface ozone in China. Proc. Natl. Acad. Sci. U. S. A. 116, 422–427.

Liu, L., Mishchenko, M.I., 2008. Toward unified satellite climatology of aerosol properties: direct comparisons of advanced level 2 aerosol products. J. Quant. Spectrosc. Radiat. Transf. 109, 2376–2385.

Liu, X., Easter, R.C., Ghan, S.J., Zaveri, R., Rasch, P., Shi, X., Lamarque, J.F., Gettelman, A., Morrison, H., Vitt, F., Conley, A., Park, S., Neale, R., Hannay, C., Ekman, A.M.L., Hess, P., Mahowald, N., Collins, W., Iacono, M.J., Bretherton, C.S., Flanner, M.G., Mitchell, D., 2012. Toward a minimal representation of aerosols in climate models: description and evaluation in the community atmosphere model CAM5. Geosci. Model Dev. 5, 709–739.

Liu, C., Chen, R., Sera, F., Vicedo-Cabrera, A.M., Guo, Y., Tong, S., Coelho, M., Saldiva, P. H.N., Lavigne, E., Matus, P., Valdes Ortega, N., Osorio Garcia, S., Pascal, M., Stafoggia, M., Scortichini, M., Hashizume, M., Honda, Y., Hurtado-Diaz, M., Cruz, J., Nunes, B., Teixeira, J.P., Kim, H., Tobias, A., Iniguez, C., Forsberg, B., Astrom, C., Ragettli, M.S., Guo, Y.L., Chen, B.Y., Bell, M.L., Wright, C.Y., Scovronick, N., Garland, R.M., Milojevic, A., Kysely, J., Urban, A., Orru, H., Indermitte, E., Jaakkola, J.J.K., Ryti, N.R.I., Katsouyanni, K., Analitis, A., Zanobetti, A., Schwartz, J., Chen, J., Wu, T., 2019. Ambient Particulate Air Pollution and Daily Mortality in 652 Cities, *381*, pp. 705–715.

Livezey, R.E., Chen, W., 1983. Statistical field significance and its determination by Monte Carlo techniques. Mon. Weather Rev. 111, 46–59.

Loeb, N.G., Doelling, D.R., Wang, H., Su, W., Nguyen, C., Corbett, J.G., Liang, L., Mitrescu, C., Rose, F.G., Kato, S., 2018. Clouds and the earth's radiant energy system (CERES) energy balanced and filled (EBAF) top-of-atmosphere (TOA) edition-4.0 data product. J. Clim. 31, 895–918.

Mann, H.B., 1945. Nonparametric tests against trend. Econometrica 13, 245–259.

Marticorena, B., Bergametti, G., 1995. Modeling the Atmospheric Dust Cycle.1. Design of a Soil-Derived Dust Emission Scheme. J. Geophys. Res.-Atmos. 100, 16415–16430.

Martins, V.S., Lyapustin, A., Wang, Y.J., Giles, D.M., Smirnov, A., Slutsker, I., Korkin, S., 2019. Global validation of columnar water vapor derived from EOS MODIS-MAIAC algorithm against the ground-based AERONET observations. Atmos. Res. 225, 181–192.

Martonchik, J.V., 1997. Determination of aerosol optical depth and land surface directional reflectances using multiangle imagery. J. Geophys. Res.-Atmos. 102, 17015–17022.

Martonchik, J.V., Kahn, R.A., & Diner, D.J. (2009). Retrieval of aerosol properties over land using MISR observations. *Satellite aerosol remote sensing over land* (pp. 267-293): Springer.

McCarty, W.L., Coy, L., Gelaro, R., Huang, A., Merkova, D., Smith, E.B., Sienkiewicz, M., Wargan, K., 2016. MERRA-2 input observations: summary and assessment (NASA TM-2016-104606). NASA Global Model. Assimilation Office 46, 64 pp.

Mehta, M., Singh, R., Singh, A., Singh, N., Anshumali, 2016. Recent global aerosol optical depth variations and trends - a comparative study using MODIS and MISR level 3 datasets. Remote Sens. Environ. 181, 137–150.

Minnis, P., Trepte, Q.Z., Sun-Mack, S., Chen, Y., Doelling, D.R., Young, D.F., Spangenberg, D.A., Miller, W.F., Wielicki, B.A., Brown, R.R., 2008. Cloud detection in nonpolar regions for CERES using TRMM VIRS and Terra and Aqua MODIS data. IEEE Trans. Geosci. Remote Sens. 46, 3857–3884.

Mishchenko, M.I., Geogdzhayev, I.V., Liu, L., Lacis, A.A., Cairns, B., Travis, L.D., 2009. Toward unified satellite climatology of aerosol properties: what do fully compatible MODIS and MISR aerosol pixels tell us? J. Quant. Spectrosc. Radiat. Transf. 110, 402–408.

Mishchenko, M.I., Liu, L., Geogdzhayev, I.V., Travis, L.D., Cairns, B., Lacis, A.A., 2010. Toward unified satellite climatology of aerosol properties. 3. MODIS versus MISR versus AERONET. J. Quant. Spectrosc. Radiat. Transf. 111, 540–552.

Molod, A., Takacs, L., Suarez, M., Bacmeister, J., 2015. Development of the GEOS-5 atmospheric general circulation model: evolution from MERRA to MERRA2. Geosci. Model Dev. 8, 1339–1356.

Ningombam, S.S., Larson, E.J.L., Dumka, U.C., Estelles, V., Campanelli, M., Steve, C., 2019. Long-term (1995-2018) aerosol optical depth derived using ground based AERONET and SKYNET measurements from aerosol aged-background sites. Atmos. Pollution Res. 10, 608–620.

Pant, P., Lal, R.M., Guttikunda, S.K., Russell, A.G., Nagpure, A.S., Ramaswami, A., Peltier, R.E., 2018. Monitoring particulate matter in India: recent trends and future outlook. Air Qual. Atmos. Health 12, 45–58.

Park, R.S., Lee, S., Shin, S.K., Song, C.H., 2014. Contribution of ammonium nitrate to aerosol optical depth and direct radiative forcing by aerosols over East Asia. Atmos. Chem. Phys. 14, 2185–2201.

Pathak, H.S., Satheesh, S.K., Nanjundiah, R.S., Moorthy, K.K., Lakshmivarahan, S., Babu, S.N.S., 2019. Assessment of regional aerosol radiative effects under the SWAAMI campaign – part 1: quality-enhanced estimation of columnar aerosol extinction and absorption over the Indian subcontinent. Atmos. Chem. Phys. 19, 11865–11886.

Peng, Z., Letu, H., Wang, T., Shi, C., Zhao, C., Tana, G., Zhao, N., Dai, T., Tang, R., Shang, H., 2020. Estimation of shortwave solar radiation using the artificial neural network from Himawari-8 satellite imagery over China. J. Quant. Spectrosc. Radiat. Transf. 240, 106672.

Pokharel, M., Guang, J., Liu, B., Kang, S., Ma, Y., Holben, B.N., Xia, X.a., Xin, J., Ram, K., Rupakheti, D., 2019. Aerosol properties over Tibetan plateau from a decade of AERONET measurements: baseline, types, and influencing factors. J. Geophys. Res.-Atmos. 124, 13357–13374.

Pozzer, A., De Meij, A., Yoon, J., Tost, H., Georgoulias, A., Astitha, M., 2015. AOD trends during 2001–2010 from observations and model simulations. Atmos. Chem. Phys. 15, 5521–5535.

Prijith, S.S., Rao, P.V.N., Mohan, M., Sai, M.V.R.S., Ramana, M.V., 2018. Trends of absorption, scattering and total aerosol optical depths over India and surrounding oceanic regions from satellite observations: role of local production, transport and atmospheric dynamics. Environ. Sci. Pollut. Res. 25, 18147–18160.

Pu, B., Ginoux, P., 2016. The impact of the Pacific decadal oscillation on springtime dust activity in Syria. Atmos. Chem. Phys. 16, 13431–13448.

Qiu, Y., Zhao, C., Guo, J., Li, J., 2017. 8-year ground-based observation analysis about the seasonal variation of the aerosol's cloud albedo effect and precipitable water vapor contribution at SGP site. Atmos. Environ. 164, 139–146.

Ramachandran, S., Kedia, S., Srivastava, R., 2012. Aerosol optical depth trends over different regions of India. Atmos. Environ. 49, 338–347.

Randles, C.A., da Silva, A.M., Buchard, V., Darmenov, A., Colarco, P.R., Aquila, V., Bian, H., Nowottnick, E.P., Pan, X., Smirnov, A., Yu, H., Govindaraju, R., 2016. The MERRA-2 Aerosol Assimilation (TM–2016-104606) *NASA Global Modeling and Assimilation Office, 45*.

Randles, C.A., da Silva, A.M., Buchard, V., Colarco, P.R., Darmenov, A., Govindaraju, R., Smirnov, A., Holben, B., Ferrare, R., Hair, J., Shinozuka, Y., Flynn, C.J., 2017. The MERRA-2 aerosol reanalysis, 1980 onward. Part I: System Description and Data Assimilation Evaluation. J. Clim. 30, 6823–6850.

Remer, L.A., Kaufman, Y., Tanré, D., Mattoo, S., Chu, D., Martins, J.V., Li, R.-R., Ichoku, C., Levy, R., Kleidman, R., 2005. The MODIS aerosol algorithm, products, and validation. J. Atmos. Sci. 62, 947–973.

Remer, L.A., Kleidman, R.G., Levy, R.C., Kaufman, Y.J., Tanré, D., Mattoo, S., Martins, J. V., Ichoku, C., Koren, I., Yu, H., 2008. Global Aerosol Climatology from the MODIS Satellite Sensors. Atmospheres, Journal of Geophysical Research, p. 113.

Remer, L.A., Levy, R.C., Mattoo, S., Tanré, D., Gupta, P., Shi, Y., Sawyer, V., Munchak, L. A., Zhou, Y., Kim, M., Ichoku, C., Patadia, F., Li, R.-R., Gassó, S., Kleidman, R.G., Holben, B.N., 2020. The dark target algorithm for observing the global aerosol system: past, present, and future. Remote Sens. 12.

Rienecker, M.M., Suarez, M.J., Gelaro, R., Todling, R., Bacmeister, J., Liu, E., Bosilovich, M.G., Schubert, S.D., Takacs, L., Kim, G.K., Bloom, S., Chen, J.Y., Collins, D., Conaty, A., Da Silva, A., Gu, W., Joiner, J., Koster, R.D., Lucchesi, R., Molod, A., Owens, T., Pawson, S., Pegion, P., Redder, C.R., Reichle, R., Robertson, F. R., Ruddick, A.G., Sienkiewicz, M., Woollen, J., 2011. MERRA: NASA's modern-era retrospective analysis for research and applications. J. Clim. 24, 3624–3648.

Roxy, M.K., Ghosh, S., Pathak, A., Athulya, R., Mujumdar, M., Murtugudde, R., Terray, P., Rajeevan, M., 2017. A threefold rise in widespread extreme rain events over Central India. Nat. Commun. 8.

Samset, B.H., Lund, M.T., Bollasina, M., Myhre, G., Wilcox, L., 2019. Emerging Asian aerosol patterns. Nat. Geosci. 12, 582–584.

Satheesh, S., Krishnamoorthy, K., 2005. Radiative effects of natural aerosols: a review. Atmos. Environ. 39, 2089–2110.

Sayer, A.M., Hsu, N., Bettenhausen, C., Jeong, M.-J., Holben, B., Zhang, J., 2012. Global and regional evaluation of over-land spectral aerosol optical depth retrievals from SeaWiFS. Atmos. Measur. Techn. 5, 1761–1778.

Sayer, A.M., Munchak, L.A., Hsu, N.C., Levy, R.C., Bettenhausen, C., Jeong, M.J., 2014. MODIS collection 6 aerosol products: comparison between Aqua's e-deep blue, dark target, and "merged" data sets, and usage recommendations. J. Geophys. Res.-Atmos. 119, 13965–13989.

Sayer, A.M., Hsu, N.C., Lee, J., Kim, W.V., Dutcher, S.T., 2019. Validation, stability, and consistency of MODIS collection 6.1 and VIIRS version 1 deep blue aerosol data over land. J. Geophys. Res.-Atmos. 124, 4658–4688.

Sharma, D., Miller, R.L., 2017. Revisiting the observed correlation between weekly averaged Indian monsoon precipitation and Arabian Sea aerosol optical depth. Geophys. Res. Lett. 44, 10006–10016.

Shen, L., Zhao, C., 2020. Dominance of shortwave radiative heating in the sea-land breeze amplitude and its impacts on atmospheric visibility in Tokyo, Japan. J. Geophys. Res.-Atmos. 125.

Simes, R.J., 1986. An improved Bonferroni procedure for multiple tests of significance. Biometrika 73, 751–754.

Smirnov, A., Holben, B.N., Eck, T.F., Dubovik, O., Slutsker, I., 2000. Cloud-screening and quality control algorithms for the AERONET database. Remote Sens. Environ. 73, 337–349.

Solmon, F., Nair, V.S., Mallet, M., 2015. Increasing Arabian dust activity and the Indian summer monsoon. Atmos. Chem. Phys. 15, 8051–8064.

Storn, R., Price, K., 1997. Differential evolution–a simple and efficient heuristic for global optimization over continuous spaces. J. Glob. Optim. 11, 341–359.

Sundaray, S.N.K., Bhardwaj, S.R., 2019. National Clean air Programme. In: In (Pp. 1–122). Indian Ministry of Environment, Forest & Climate Change.

Tang, Y., Pagowski, M., Chai, T., Pan, L., Lee, P., Baker, B., Kumar, R., Delle Monache, L., Tong, D., Kim, H.-C., 2017. A case study of aerosol data assimilation with the community multi-scale air quality model over the contiguous United States using 3D-Var and optimal interpolation methods. Geosci. Model Dev. 10, 4743–4758.

van Donkelaar, A., Martin, R.V., Park, R.J., 2006. Estimating ground-level PM2.5using aerosol optical depth determined from satellite remote sensing. J. Geophys. Res. *111*.

van Donkelaar, A., Martin, R.V., Brauer, M., Kahn, R., Levy, R., Verduzco, C., Villeneuve, P.J., 2010. Global estimates of ambient fine particulate matter concentrations from satellite-based aerosol optical depth: development and application. Environ. Health Perspect. 118, 847–855.

van Donkelaar, A., Martin, R.V., Brauer, M., Hsu, N.C., Kahn, R.A., Levy, R.C., Lyapustin, A., Sayer, A.M., Winker, D.M., 2016. Global estimates of fine particulate matter using a combined geophysical-statistical method with information from satellites, models, and monitors. Environ. Sci. Technol. 50, 3762–3772.

Vinoj, V., Rasch, P.J., Wang, H.L., Yoon, J.H., Ma, P.L., Landu, K., Singh, B., 2014. Short-term modulation of Indian summer monsoon rainfall by west Asian dust. Nat. Geosci. 7, 308–313.

Wang, Y., Zhao, C., 2017. Can MODIS cloud fraction fully represent the diurnal and seasonal variations at DOE ARM SGP and Manus sites? J. Geophys. Res.-Atmos. 122, 329–343.

Wang, Q., Li, Z., Guo, J., Zhao, C., Cribb, M., 2018. The climate impact of aerosols on the lightning flash rate: is it detectable from long-term measurements? Atmos. Chem. Phys. 18, 12797–12816.

Weagle, C.L., Snider, G., Li, C., van Donkelaar, A., Philip, S., Bissonnette, P., Burke, J., Jackson, J., Latimer, R., Stone, E., Abboud, I., Akoshile, C., Anh, N.X., Brook, J.R., Cohen, A., Dong, J., Gibson, M.D., Griffith, D., He, K.B., Holben, B.N., Kahn, R., Keller, C.A., Kim, J.S., Lagrosas, N., Lestari, P., Khian, Y.L., Liu, Y., Marais, E.A., Martins, J.V., Misra, A., Muliane, U., Pratiwi, R., Quel, E.J., Salam, A., Segev, L., Tripathi, S.N., Wang, C., Zhang, Q., Brauer, M., Rudich, Y., Martin, R.V., 2018. Global Sources of Fine Particulate Matter: Interpretation of PM2.5 Chemical Composition Observed by SPARTAN using a Global Chemical Transport Model. Environ. Sci. Technol. 52, 11670–11681.

Wei, J., Peng, Y.R., Mahmood, R., Sun, L., Guo, J.P., 2019. Intercomparison in spatial distributions and temporal trends derived from multi-source satellite aerosol products. Atmos. Chem. Phys. 19, 7183–7207.

Wielicki, B.A., Barkstrom, B.R., Harrison, E.F., Lee III, R.B., Smith, G.L., Cooper, J.E., 1996. Clouds and the Earth's radiant energy system (CERES): An earth observing system experiment. Bull. Am. Meteorol. Soc. 77, 853–868.

Wilks, D.S., 2006. On "field significance" and the false discovery rate. J. Appl. Meteorol. Climatol. 45, 1181–1189.

Wilks, D.S., 2016. "THE STIPPLING SHOWS STATISTICALLY SIGNIFICANT GRID POINTS" how research results are routinely overstated and Overinterpreted, and what to do about it. Bull. Am. Meteorol. Soc. 97, 2263–2273.

Xie, Y., Xue, Y., Guang, J., Mei, L., She, L., Li, Y., Che, Y., Fan, C., 2020. Deriving a global and hourly data set of aerosol optical depth over land using data from four geostationary satellites: GOES-16, MSG-1, MSG-4, and Himawari-8. IEEE Trans. Geosci. Remote Sens. 58, 1538–1549.

Yang, X., Zhao, C., Zhou, L., Li, Z., Cribb, M., Yang, S., 2018a. Wintertime cooling and a potential connection with transported aerosols in Hong Kong during recent decades. Atmos. Res. 211, 52–61.

Yang, Y., Wang, H.L., Smith, S.J., Zhang, R.D., Lou, S.J., Yu, H.B., Li, C., Rasch, P.J., 2018b. Source apportionments of aerosols and their direct Radiative forcing and long-term trends over continental United States. Earths Future 6, 793–808.

Yang, Y., Zhao, C., Sun, L., Wei, J., 2019. Improved aerosol retrievals over complex regions using NPP visible infrared imaging radiometer suite observations. Earth Space Sci. 6, 629–645.

Yang, X., Zhao, C., Luo, N., Zhao, W., Shi, W., Yan, X., 2020. Evaluation and comparison of Himawari-8 L2 V1. 0, V2. 1 and MODIS C6. 1 aerosol products over Asia and the oceania regions. Atmos. Environ. 220, 117068.

Yu, H., Yang, Y., Wang, H., Tan, Q., Chin, M., Levy, R.C., Remer, L.A., Smith, S.J., Yuan, T., Shi, Y., 2020. Interannual variability and trends of combustion aerosol and dust in major continental outflows revealed by MODIS retrievals and CAM5 simulations during 2003–2017. Atmos. Chem. Phys. 20, 139–161. https://doi.org/10.5194/acp-20-139-2020.

Zhai, S., Jacob, D.J., Wang, X., Shen, L., Li, K., Zhang, Y., Gui, K., Zhao, T., Liao, H., 2019. Fine particulate matter (PM2.5) trends in China, 2013–2018: separating contributions from anthropogenic emissions and meteorology. Atmos. Chem. Phys. 19, 11031–11041.

Zhang, J., Reid, J.S., 2010. A decadal regional and global trend analysis of the aerosol optical depth using a data-assimilation grade over-water MODIS and level 2 MISR aerosol products. Atmos. Chem. Phys. 10, 10949–10963.

Zhang, K., Zhao, C., Fan, H., Yang, Y., Sun, Y., 2019a. Toward understanding the differences of PM 2.5 characteristics among five China urban cities. Asia-Pac. J. Atmos. Sci. 1–10.

Zhang, Q., Zheng, Y., Tong, D., Shao, M., Wang, S., Zhang, Y., Xu, X., Wang, J., He, H., Liu, W., Ding, Y., Lei, Y., Li, J., Wang, Z., Zhang, X., Wang, Y., Cheng, J., Liu, Y., Shi, Q., Yan, L., Geng, G., Hong, C., Li, M., Liu, F., Zheng, B., Cao, J., Ding, A., Gao, J., Fu, Q., Huo, J., Liu, B., Liu, Z., Yang, F., He, K., Hao, J., 2019b. Drivers of improved PM2.5 air quality in China from 2013 to 2017. Proc. Natl. Acad. Sci. U. S. A. 116, 24463–24469.

Zhao, B., Jiang, J.H., Gu, Y., Diner, D., Worden, J., Liou, K.N., Su, H., Xing, J., Garay, M., Huang, L., 2017. Decadal-scale trends in regional aerosol particle properties and their linkage to emission changes. Environ. Res. Lett. 12.

Zhao, C., Qiu, Y., Dong, X., Wang, Z., Peng, Y., Li, B., Wu, Z., Wang, Y., 2018. Negative aerosol-cloud rerelationship from aircraft observations over Hebei, China. Earth Space Sci. 5, 19–29.

Zhao, C., Wang, Y., Shi, X., Zhang, D., Wang, C., Jiang, J.H., Zhang, Q., Fan, H., 2019. Estimating the contribution of local primary emissions to particulate pollution using high-density station observations. J. Geophys. Res.-Atmos. 124, 1648–1661.

Zhao, C., Yang, Y., Fan, H., Huang, J., Fu, Y., Zhang, X., Kang, S., Cong, Z., Letu, H., Menenti, M., 2020. Aerosol characteristics and impacts on weather and climate over the Tibetan plateau. Natl. Sci. Rev. 7, 492–495.

Zwiers, F.W., Von Storch, H., 1995. Taking serial correlation into account in tests of the mean. J. Clim. 8, 336–351.